Atmos. Chem. Phys. Discuss., 13, 18621–18677, 2013
www.atmos-chem-phys-discuss.net/13/18621/2013/
doi:10.5194/acpd-13-18621-2013


Atmospheric Chemistry and Physics Discussions



# Projected effects of declining aerosols in RCP4.5: unmasking global warming?

**L. D. Rotstayn[1], M. A. Collier[1], A. Chrastansky[1], S. J. Jeffrey[2], and J.-J. Luo[3]**

[1]Centre for Australian Weather and Climate Research, CSIRO Marine and Atmospheric Research, Aspendale, Vic, Australia
[2]Department of Science, Information Technology, Innovation and the Arts, Dutton Park, Qld, Australia
[3]Centre for Australian Weather and Climate Research, Bureau of Meteorology, Melbourne, Vic, Australia

Received: 21 June 2013 – Accepted: 27 June 2013 – Published: 11 July 2013

Correspondence to: L. D. Rotstayn (leon.rotstayn@csiro.au)

Published by Copernicus Publications on behalf of the European Geosciences Union.







## Abstract

All the Representative Concentration Pathways (RCPs) include declining aerosol emissions during the 21st century, but the effects of these declines on climate projections have had little attention. Here we assess the global and hemispheric-scale effects of declining anthropogenic aerosols in RCP4.5 in CSIRO-Mk3.6, a model from the Coupled Model Intercomparison Project Phase 5 (CMIP5). Results from this model are then compared with those from other CMIP5 models.

We calculate the aerosol effective radiative forcing (ERF, including indirect effects) in CSIRO-Mk3.6 relative to 1850, using a series of atmospheric simulations with prescribed sea-surface temperatures. Global-mean aerosol ERF at the top of the atmosphere is most negative in 2005 ($-1.47\,W\,m^{-2}$). Between 2005 and 2100 it increases by $1.46\,W\,m^{-2}$, i.e., it approximately returns to 1850 levels. Although increasing greenhouse gases (GHGs) and declining aerosols both exert a positive ERF at the top of the atmosphere during the 21st century, they have opposing effects on radiative heating of the atmosphere: increasing GHGs warm the atmosphere, whereas declining aerosols cool the atmosphere due to reduced absorption of shortwave radiation by black carbon.

We then compare two projections for 2006–2100, using the coupled atmosphere-ocean version of the model. One (RCP45) follows the usual RCP4.5; the other (RCP45A2005) has identical forcing, except that emissions of anthropogenic aerosols and precursors are fixed at 2005 levels. The global-mean surface warming in RCP45 is 2.3 °C per 95 yr, of which almost half (1.1 °C) is caused by declining aerosols. The warming due to declining aerosols is almost twice as strong in the Northern Hemisphere as in the Southern Hemisphere, whereas that due to increasing GHGs is similar in the two hemispheres.

For precipitation changes, the effects of declining aerosols are larger than those of increasing GHGs due to decreasing atmospheric absorption by black carbon: 63 % of the projected global-mean precipitation increase of 0.16 mm per day is caused by






ACPD
13, 18621–18677, 2013



declining aerosols. In the Northern Hemisphere, precipitation increases by 0.29 mm per day, of which 72 % is caused by declining aerosols.

Using data from 13 CMIP5 models, we find that projected global-mean surface warming in RCP4.5 is systematically larger in models that have more negative aerosol ERF in the present climate ($r = -0.54$, $p = 0.03$). A similar correlation is found for global-mean precipitation changes ($r = -0.56$, $p = 0.02$).

These results suggest that aerosol forcing substantially modulates projected climate response in RCP4.5. In some respects, the effects of declining aerosols are quite distinct from those of increasing GHGs. Systematic efforts are needed to better quantify the role of declining aerosols in climate projections.

## 1 Introduction

It has been broadly understood for more than two decades that anthropogenic aerosols (AAs) have masked the warming effects of increasing greenhouse gases, and that efforts to reduce aerosol concentrations are likely to exacerbate future increases of global-mean temperature (Wigley, 1989). However, aerosol effects are very uncertain, especially when aerosol indirect effects are considered. For example, just for the cloud-albedo effect in liquid-water clouds (the first indirect effect), Forster et al. (2007) gave an estimated 95 % uncertainty range of $-0.3$ to $-1.8\,\mathrm{W\,m^{-2}}$ in the global mean.

In the Coupled Model Intercomparison Project Phase 5 (CMIP5; Taylor et al., 2012), future projections are based on four Representative Concentration Pathways (RCPs). A feature of all of these is that emissions of aerosols and aerosol precursors decline sharply in the 21st century (Lamarque et al., 2011). Although some of the the earlier Special Report on Emissions Scenarios (SRES; Nakicenovic et al., 2000) did incorporate substantial decreases in sulfur dioxide emissions, these decreases are much larger in the RCPs (Van Vuuren et al., 2011). Combined with an increase in the number of models that treat indirect aerosol effects, this may translate into a larger inter-model spread of projected climate change in CMIP5 than in CMIP3. This has already been





ACPD
13, 18621–18677, 2013



noted with regard to historical simulations: Jones et al. (2013) found a wider spread of simulated historical temperature changes in CMIP5 than in CMIP3, and attributed this to more sophisticated aerosol treatments in the newer models.

Most simulations of the effects of AAs on climate have focused on the historical period, when AAs have generally been increasing. A key finding from these studies is that aerosols cannot be characterised as a "negative greenhouse gas", which simply masks some of the effects of increasing long-lived greenhouse gases (GHGs). Aerosol forcing is spatially inhomogeneous, and this can induce dynamic effects on circulation due to gradients in the forcing (Rotstayn and Lohmann, 2002a). In terms of large-scale circulation, the dynamic effect of historically increasing aerosol has been described as a southward shift of the intertropical convergence zone (Rotstayn et al., 2000; Williams et al., 2001), or a weakening of the upward branch of the Hadley circulation in the Northern Hemisphere (NH) and a strengthening of the upward branch in the Southern Hemisphere (SH) (Ming and Ramaswamy, 2011). These changes can be explained as the response to a change in the meridional surface temperature gradient (Rotstayn et al., 2000; Williams et al., 2001), or the inter-hemispheric asymmetry in aerosol forcing, for which the atmospheric circulation partially compensates (Kang et al., 2009; Ming and Ramaswamy, 2011; Chiang and Friedman, 2012).

Climate modelling also suggests large regional impacts on circulation and rainfall from historical increases in AAs. There is evidence that AA-induced circulation changes have affected rainfall in South Asia (Ramanathan et al., 2005; Meehl et al., 2008; Bollasina et al., 2011), East Asia (Menon et al., 2002; Cheng et al., 2005; Liu et al., 2011) and the Sahel (Rotstayn and Lohmann, 2002a; Kawase et al., 2010; Ackerley et al., 2011). Booth et al. (2012) found that in the HadGEM2-ES climate model, aerosols were the most important driver of 20th century North Atlantic SST variability, although Chiang and Friedman (2012) concluded that the relative importance of natural variability and anthropogenic forcing is still uncertain. Most studies of these effects have focused on the NH, but there is also evidence that changes in AAs can alter circulation in the SH (e.g., Rotstayn et al., 2012, 2013).





ACPD
13, 18621–18677, 2013



Such large effects in simulations of historical changes in AAs suggest that there will also be substantial effects due to declining aerosols in 21st century projections. Prior to CMIP5, Kloster et al. (2010) found substantial effects on temperature and precipitation due to a maximum feasible abatement of aerosols in near-term (2030) climate projections. The effects of declining aerosols in 21st century projections in CMIP5 are likely to be larger than they were in CMIP3, due to larger decreases of emissions, and an increase in the proportion of models that include indirect aerosol effects (e.g., Levy et al., 2013). Chalmers et al. (2012) found that the near-term warming projected under RCP2.6 in the HadGEM2-ES model is greater than under RCP4.5, even though the greenhouse-gas forcing is weaker in RCP2.6; they attributed the greater warming to a rapid and substantial decrease of sulfur emissions in RCP2.6.

The above arguments indicate a need for a systematic effort to quantify the role of declining AAs in projections of 21st century climate. A similar point was made by Villarini and Vecchi (2012). They found that over the first half of the 21st century, radiative forcing changes increased the frequency of tropical cyclones over the North Atlantic in CMIP5 projections, and this increase probably arose from decreasing aerosols. They also highlighted the need for coordinated experiments that isolate the effects of different forcing agents, because they were unable to test this hypothesis across the full set of CMIP5 models.

The most direct way to isolate the effects of projected aerosol changes is to run simulations that are similar to the standard RCPs, except that AA emissions are held fixed. This approach was recently adopted by Levy et al. (2013), who compared simulations forced by RCP4.5 with a modified RCP4.5 in which AA emissions were fixed at their 2005 values. Among other things, they found that declining aerosols in their model caused about 1 °C of extra warming by 2100 in RCP4.5.

Here we consider the effects of declining aerosols in RCP4.5 in a CMIP5 climate model (CSIRO-Mk3.6), by comparing two projections for the period 2006–2100. One experiment follows the usual RCP4.5, whereas the other has identical forcing, except that emissions of AAs and their precursors are held fixed at 2005 levels; the differ-





ACPD
13, 18621–18677, 2013



ence between these two experiments gives the simulated effects of declining AAs. We assess the aerosol radiative forcing and compare global and hemispheric-scale changes in surface temperature and precipitation induced by declining AAs and increasing greenhouse gases. We also assess these changes in other CMIP5 models for which calculations of aerosol radiative forcing are available.

## 2 Model and simulations

### 2.1 Model description

CSIRO Mark 3.6 (CSIRO-Mk3.6) is a coupled atmosphere-ocean global climate model (GCM) with dynamic sea ice. The main differences between Mk3.6 and its predecessor (Mk3.5) are the inclusion of an interactive aerosol treatment, an updated radiation scheme, and a revised boundary-layer scheme in Mk3.6. The aerosol scheme treats sulfate, organic aerosol (OA), black carbon (BC), dust and sea salt. The model and the forcing data used for CMIP5 are described by Rotstayn et al. (2012), with a particular focus on the aerosol treatments; earlier versions are described in detail by Gordon et al. (2002, 2010). The ocean and sea-ice models are unchanged between Mk3.5 and Mk3.6.

Here we briefly describe aspects of the aerosol scheme that are most relevant to the present study. Although feedbacks involving dust and sea salt can occur, our focus is mainly on the anthropogenic species, so readers are referred to Rotstayn et al. (2012) for further details of the dust and sea-salt treatments. Carbonaceous aerosols and the sulfur cycle are treated by a single-moment ("bulk") prognostic scheme: tracers are the mass mixing ratios of dimethyl sulfide (DMS), sulfur dioxide ($SO_2$), sulfate, and hydrophobic and hydrophilic forms of OA and BC. The treatment of tropospheric sulfur chemistry is based on Feichter et al. (1996) and Rotstayn and Lohmann (2002b). Oxidant fields needed for the sulfur cycle are prescribed for the present climate (Feichter et al., 1996). The carbonaceous aerosol module (Cooke et al., 1999) is rather simple,





ACPD
13, 18621–18677, 2013



and does not explicitly treat chemical reactions; rather, it assumes a fixed e-folding time of 1 day for the "ageing" of OA and BC from their hydrophobic to hydrophilic forms. The ratio of OA to organic carbon is set to 1.3.

Anthropogenic and biomass-burning emissions of sulfur, OA and BC are based on Lamarque et al. (2010, 2011), except that we uniformly increased the emissions of BC by 25 % and OA by 50 % (Rotstayn et al., 2012). We justified the BC increase by the large uncertainty in current emission inventories, and the underestimate of aerosol atmospheric heating in current GCMs (e.g., Shindell et al., 2013a). The rationale for the OC increase was the model's underestimate of aerosol optical depth (AOD) in biomass-burning regions, and the omission of secondary OA from biomass burning and anthropogenic sources in the standard inventory; such secondary aerosol formation can substantially enhance effective emissions of OA (e.g., Lee et al., 2008). After these adjustments, the annual year-2000 emission of BC is 9.7 Tg, and the emission of OA from biomass-burning and anthropogenic sources is 53 Tg C, both well within the uncertainty range of current estimates.

The model also includes natural sources, which are mostly constant in time. Natural sources of sulfur are $SO_2$ from continuously erupting volcanoes and biogenic emissions of DMS from oceans and terrestrial sources. The only natural source of carbonaceous aerosol is a prescribed flux of biogenic secondary organic aerosol (Guenther et al., 1995; Rotstayn et al., 2012). Note that the oceanic DMS source is not constant in time; even though the concentration of DMS in sea water is prescribed (Kettle and Andreae, 2000), the ocean-atmosphere flux of DMS is wind-dependent.

CSIRO-Mk3.6 treats the direct radiative effects of sulfate, carbonaceous aerosol (OA and BC), dust and sea salt and the indirect effects of sulfate, sea salt and carbonaceous aerosol on liquid-water clouds. In the radiation scheme, OA and BC are assumed to be internally mixed, while other aerosol species are externally mixed. The model also includes treatments of the first and second aerosol indirect effects on liquid-water clouds. The parameterisation of cloud droplet number concentration as a function of the concentration of hydrophilic aerosols is based on Jones et al. (2001); hydrophilic aerosols





ACPD
13, 18621–18677, 2013



are assumed to be sulfate, sea salt and (internally mixed) hydrophilic carbonaceous aerosol. The calculation of the first indirect effect follows Rotstayn and Liu (2009). The second indirect aerosol effect (sometimes called the cloud-lifetime effect) enters the model via the calculation of warm-rain formation (autoconversion) in liquid-water stratiform clouds (Rotstayn and Liu, 2005). Note that the calculation of cloud fraction, and ice-cloud properties in general, do not depend on aerosols in any way (Rotstayn, 1997, 1999). Further details of the treatments of aerosol-radiation and aerosol-cloud interactions are given by Rotstayn et al. (2007, 2012).

Rotstayn et al. (2012) evaluated the present-day aerosol simulation with regard to observations and other models. They found that the global-mean aerosol burdens and anthropogenic AODs in the CSIRO-Mk3.6 yr-2000 simulation from CMIP5 were larger than the average of earlier models, though they were not outside the range of these results. In a recent intercomparison, Shindell et al. (2013a) found that mid-visible, clear-sky (all-sky) AODs in CSIRO-Mk3.6 were biased high with respect to satellite retrievals, by an average of 21 % (13 %) compared to MODIS and 16 % (7 %) compared to MISR. Some of the high bias is likely due to large dust AODs, rather than anthropogenic AODs (Rotstayn et al., 2011). Two other models also showed a high bias relative to satellite-retrieved AODs, whereas five models showed a low bias. Considering the spatial pattern, CSIRO-Mk3.6 clear-sky AODs had correlations with MODIS and MISR retrievals of 0.62 and 0.64, respectively, which was slightly better than the average of the other models in Shindell et al. (2013a).

## 2.2 Simulations

A substantial number of transient experiments were performed with CSIRO-Mk3.6 as part of CMIP5 (Jeffrey et al., 2013); these included the standard historical experiment with "all forcings", a range of historical experiments driven by changes in individual forcing agents, and projections driven by the four RCPs. Here we use the following experiments, each of which is a 10-member ensemble:





ACPD
13, 18621–18677, 2013



– HIST: standard historical run for 1850–2005 with "all forcings", namely long-lived GHGs, ozone, AAs, volcanic and solar forcing.

– RCP45: projection for 2006 to 2100 based on RCP4.5, a medium-low emission pathway in which total radiative forcing is stabilized before 2100 at roughly 4.5 $W\,m^{-2}$ (Thomson et al., 2011); further details are given in the next paragraph.

– RCP45A2005: same as RCP45, except that emissions of AAs and their precursors are held fixed at 2005 values. (To simplify the terminology, AAs include aerosols from biomass burning.)

RCP45 is forced by changes in (1) annual-mean concentrations of long-lived GHGs (carbon dioxide, methane, nitrous oxide and chlorofluorocarbons), (2) annual-mean concentrations of ozone (Cionni et al., 2011), and (3) emissions of AAs and their precursors ($SO_2$, OA and BC). There is also a simple representation of the 11 yr solar cycle, and a small implied positive forcing (relative to the historical period) due to the assumption of zero volcanic forcing after 2000. Further details of the experimental design and radiative forcings are given by Rotstayn et al. (2012) and Jeffrey et al. (2013).

RCP45A2005 has not been published as part of the CSIRO-Mk3.6 CMIP5 submission, but it uses the same code and experimental design as the other experiments. We shall refer to climatic changes in RCP45A2005 as "GHG-induced", noting that this includes the effects of increasing long-lived GHGs and changes in tropospheric and stratospheric ozone concentrations. Changes in tropospheric ozone are relatively small in RCP4.5 (Shindell et al., 2013a). While the recovery of stratospheric ozone can be important for mid-latitude dynamics, especially in the SH (Arblaster et al., 2011), we expect the effects to be modest for global and hemispheric-scale changes in temperature and precipitation, which is our main focus here.

The effects of declining AAs are diagnosed from RCP45 minus RCP45A2005. Some aspects of the response are likely to be non-linear, in the sense that RCP45 minus RCP45A2005 is not identical to an experiment forced only by declining AAs after 2005;





ACPD
13, 18621–18677, 2013



this has been seen for historical changes of AAs in atmospheric models coupled to slab ocean models (Feichter et al., 2004; Ming and Ramaswamy, 2009).

We will refer, in passing, to the following transient experiments, which are also 10-member ensembles:

- RCP26, RCP60 and RCP85: projections forced by the other three RCPs.
- NoAA: same as HIST, except that emissions of AAs and their precursors are held fixed at 1850 values. This experiment was extended from 2006 to 2012 using assumptions from RCP45, i.e., all forcing agents varied as in RCP45, except for AAs.

We also carried out several simulations with prescribed SSTs, designed to calculate radiative forcing for different years; these runs are similar to those used in CMIP5 to calculate aerosol forcing for 2000 relative to 1850, and are described in more detail in Sect. 3.2.

## 3 Aerosol changes and radiative forcing

### 3.1 Aerosol changes

Whereas aerosol emissions, burdens and AODs generally increased in magnitude during the 20th century, the converse applies in 21st century projections. Time series of these quantities are shown in Fig. 1.

Global anthropogenic emissions of $SO_2$, OA and BC are shown in Fig. 1a, with BC multiplied by 10 for clarity. $SO_2$ shows the steepest increase until the 1970 s, when emission controls in developed countries began to take effect (Smith et al., 2011). The increase between 2000 and 2005 is mostly due to economic growth in China (Klimont et al., 2013). Both $SO_2$ and BC emissions peak in 2005 and show steep declines in the 21st century in RCP45, due to assumed decreases once national incomes reach a certain level (Smith and Bond, 2013). By 2100, global emissions of $SO_2$ and BC





ACPD
13, 18621–18677, 2013



are similar to what they were in 1900. OA emissions are dominated by open biomass burning; in relative terms the rise and fall of OA emissions appears less dramatic, although by 2100 OA emissions are slightly below their 1850 value.

Simulated time series of global burdens of sulfate, OA and BC are shown in Fig. 1b, both for the historical period and the 21st century. These are broadly consistent with the corresponding emissions, e.g., sulfate shows the steepest rise until the 1970s and declines sharply in the 21st century. By 2100, sulfate and BC burdens are at levels comparable to those in 1900, whereas the OA burden is slightly below its 1850 value.

Also shown in Fig. 1b (as thin lines) are time series of global aerosol burdens in RCP45A2005. Reflecting constant anthropogenic emissions, global aerosol burdens are almost (but not entirely) flat during 2006–2100. Over 95 yr, OA shows a decrease of ∼ 1 %, and sulfate shows a decrease of ∼ 3 %. Use of fixed anthropogenic emissions in RCP45A2005 does not guarantee that aerosol burdens and AODs will be constant in time, even in the global mean. Aerosol burdens will be affected by changes in formation, transport and removal processes (especially rainfall). Because the treatment of carbonaceous aerosol in the model is simple, rainfall is expected to be the main relevant feedback process. The balance is more complex for sulfate, because in-cloud oxidation of $SO_2$ is an important source of sulfate. Thus while scavenging by rainfall removes sulfate, formation of sulfate is enhanced in cloudier regions, which tend to be associated with more rainfall. The net result (for both sulfate and OA burdens) is a complex pattern of relatively small increases and decreases (not shown). As discussed below, the implications for changes in AOD are also relatively small.

Sub-micron AOD (defined here as the sum of AOD from sulfate, OA and BC) is useful as an integrated measure of changes in these aerosol species; it is a good predictor of direct radiative forcing, but not of indirect forcing (Shindell et al., 2013a). The red curve in Fig. 1c shows time series of global-mean sub-micron AOD from HIST and RCP45. For comparison, the same field is also shown from experiments forced by the other RCPs, and from RCP45A2005. Until about 2060, RCP45 tends to lie in between RCP26 and RCP85, although by 2100 RCP45 has the lowest AOD (slightly lower than





ACPD
13, 18621–18677, 2013



RCP26). After about 2030, the outlier is RCP60, which has a relatively weak decline in sub-micron AOD.

With fixed anthropogenic emissions, RCP45A2005 shows a small decline in global-mean sub-micron AOD (~ 4 % during 2006–2100). This is a little larger than the relative declines in the sulfate and OA burdens, most likely due to changes in simulated relative humidity: AOD for sulfate and hydrophilic carbonaceous aerosol increases with relative humidity in the model, and Mk3.6 simulates a decrease of near-surface relative humidity over most land areas (not shown). This is a common feature of climate projections forced by increasing long-lived GHGs, and is probably related to the land-ocean contrast in surface warming (O'Gorman and Muller, 2010; Sherwood et al., 2010).

Figure 2 shows the spatial pattern of trends in sub-micron AOD from RCP45 and RCP45A2005. In RCP45 (panel a), negative AOD trends are largest over and downwind of Asia and Eastern Europe, and to a lesser extent the eastern US. Trends are much smaller over the SH than the NH, although the signature of biomass burning is noticeable over Africa, South America and the Indonesian region. As expected, sub-micron AOD trends in RCP45A2005 (panel b) are much smaller, with only a few isolated areas showing decreases between 0.02 and 0.05 per century. These generally occur over the most polluted regions, where trends in RCP45 are much larger. In view of this, and to simplify our arguments, we will assume that trends in AAs in RCP45A2005 can be neglected.

### 3.2 Radiative forcing

Calculations of aerosol radiative forcing help to put the simulated response (discussed in Sect. 4) in context. We followed the method from CMIP5 by running a series of 30 yr atmospheric simulations forced by prescribed SSTs and sea ice taken as a long-term average from the pre-industrial control run. To calculate aerosol forcing, all forcing agents (other than AAs) were held at 1850 values, while emissions of AAs and their precursors were in turn set to values for the appropriate year. We did runs with AA emissions for the years 1850, 1930, 1980, 2000, 2005, 2030, 2060 and 2100, respectively





ACPD
13, 18621–18677, 2013



(following RCP4.5 after 2005). There is one minor difference in the experimental setup compared to to the runs used for CMIP5: whereas no spinup period was specified in the CMIP5 experimental design (Taylor et al., 2012), the current runs have a six-month spinup. Since aerosols have an atmospheric lifetime of a few days to weeks, this allows ample time for aerosol burdens to adjust in response to changes in emissions.

The difference in the net radiative flux at the top of the atmosphere (TOA) between the 1850 simulation and the simulation using AA and precursor emissions for a given year gives an estimate of the aerosol effective radiative forcing (ERF), which includes indirect effects and rapid adjustments induced by aerosol changes (Shindell et al., 2013a). We also calculated aerosol direct radiative forcing for each of the listed years using a double call to the shortwave radiation scheme; one call uses aerosols for the year in question, and the other call uses zero aerosols. The same approach as used for the TOA can be applied to obtain ERF or direct radiative forcing at the surface; then the difference between the TOA and surface forcing gives the atmospheric radiative heating.

While global-mean TOA ERF is useful as a predictor of global-mean temperature change, atmospheric radiative heating is important for understanding changes in global precipitation. This is because the precipitation response includes a fast atmospheric adjustment to the radiative forcing, plus a slower response that is roughly proportional to temperature change (Andrews et al., 2010). The fast precipitation response is negative for forcing agents that cause positive atmospheric radiative heating, such as increasing long-lived GHGs or BC, because the atmosphere adjusts to the perturbation by reducing the release of latent heat associated with precipitation ($L\Delta P$; Andrews et al., 2010; Ming et al., 2010). The slow increase of precipitation with increasing temperature occurs because a warmer atmosphere loses energy by increased emission of longwave radiation. In this case, the atmosphere substantially adjusts to the radiative perturbation by increasing the release of latent heat ($L\Delta P$) (Allen and Ingram, 2002; Ming et al., 2010; O'Gorman et al., 2012; Allan et al., 2013).





ACPD
13, 18621–18677, 2013



For historically increasing aerosols, both the fast and slow responses act to decrease global-mean precipitation (Ming et al., 2010). As a consequence, the hydrological sensitivity (the change in global-mean precipitation per unit change in global-mean surface temperature) is larger for aerosol forcing than for long-lived GHG forcing. This has also been discussed in the context of declining aerosols in near-term climate projections (Kloster et al., 2010).

Surface radiative forcing is also an important indicator of changes in the hydrological cycle (e.g., Roderick and Farquhar, 2002). In particular, changes in net radiation at the surface are substantially offset by changes in the latent heat flux, which in turn are linked to changes in global precipitation (Liepert et al., 2004; Andrews et al., 2009; Kloster et al., 2010). This is another way to explain the larger hydrological sensitivity for aerosol forcing compared to long-lived GHG forcing.

For comparison with the aerosol ERF, we also calculated ERF due to changes in long-lived GHGs for 2005 and 2100. These runs are analogous to the runs used to calculate aerosol forcing: concentrations of long-lived GHGs are set to values for 2005 or 2100, respectively, while other anthropogenic forcings (aerosol emissions and ozone concentrations) are held at 1850 levels.

Global- and hemispheric-mean values of aerosol ERF (relative to 1850) are plotted in Fig. 3 for 1930, 1980, 2000, 2005, 2030, 2060 and 2100. The global-mean aerosol ERF in 2000 is $-1.40 \pm 0.09\,\mathrm{W\,m^{-2}}$ (where the error range denotes a 95 % confidence interval based on a *t* test). As discussed in Sect. 5, nine other CMIP5 models that include indirect aerosol effects have global-mean aerosol ERF ranging from $-0.76\,\mathrm{W\,m^{-2}}$ to $-1.64\,\mathrm{W\,m^{-2}}$. This indicates that CSIRO-Mk3.6 has stronger than average aerosol ERF, though it is well within the range of results from CMIP5 models.

Global-mean aerosol ERF is most negative in 2005, when it reaches $-1.47\,\mathrm{W\,m^{-2}}$. Relative to 2005, global-mean aerosol ERF is $+1.46\,\mathrm{W\,m^{-2}}$ in 2100, i.e., it has roughly returned to its 1850 value. Note that aerosol ERF continues to become more positive after 2060, consistent with declining emissions and burdens (Fig. 1). This differs from





ACPD
13, 18621–18677, 2013



the nominal RCP4.5 radiative forcing, which is fairly flat after 2060 (Thomson et al., 2011, their Fig. 2), because aerosol indirect effects were not included in their modelling.

With reference to Fig. 1, we note that global $SO_2$ and BC emissions and sulfate and BC burdens are somewhat higher in 2100 than in 1850, whereas global OA emissions and burden are lower in 2100 than 1850. Thus the effect of sulfate alone would be to give a net negative ERF in 2100 relative to 1850, whereas OA and BC would give a net positive ERF (assuming negative ERF from OA, and positive ERF from BC). This suggests that OA and BC changes contribute to the return of aerosol ERF to its 1850 value by 2100. Since OA emissions in CSIRO-Mk3.6 are scaled by a factor of 1.5, the effect of OA may be relatively larger than in other models. Also, as discussed by Rotstayn et al. (2012), inclusion of hydrophilic OA in the aerosol mass concentration used in parameterization of the cloud droplet concentration implies a substantial indirect aerosol effect due to OA. This effect may be over-estimated in our runs, given that the hygroscopicity of aged biomass-burning aerosol (which is substantially comprised of OA) is generally smaller than that of sulfate (Andreae and Rosenfeld, 2008).

As previously mentioned, stronger aerosol effects in 2005 than 2000 are mostly due to increased emissions from China; this is reflected in the NH time series in Fig. 3, with a change from $-1.72\,W\,m^{-2}$ in 2000 to $-2.02\,W\,m^{-2}$ in 2005. Aerosol ERF is generally more negative in the NH than the SH, but the difference decreases during the 21st century. By 2100, aerosol ERF in both hemispheres is similar to the respective 1850 values.

How does the spatial pattern of aerosol ERF compare in the future and historical periods? Figure 4 shows aerosol ERF for 2005 (relative to 1850), and 2100 (relative to 2005). In 2005, aerosol ERF is mostly negative, except for regions where the impact of BC on surface albedo is the dominant effect (the Arctic, and a smaller area over the Himalayas). Future changes in aerosol ERF resemble the inverse of the historical pattern. Some differences are evident, e.g. future positive ERF over Africa is weaker than historical negative ERF. As in the multi-model mean from the Atmospheric Chemistry and Climate Model Intercomparison Project (ACCMIP; Shindell et al., 2013a, their





ACPD
13, 18621–18677, 2013



Fig. 18), aerosol ERF is strong over the North Pacific, where advected aerosols interact with susceptible marine clouds.

Radiative forcing changes between 2005 and 2100 at the TOA, surface and in the atmosphere are summarised in Fig. 5 for aerosols and long-lived GHGs. For clarity, we omit ozone forcing, which is relatively small in RCP4.5 (Shindell et al., 2013a). At the TOA, global-mean ERF due to increasing long-lived GHGs is $+1.54\,W\,m^{-2}$, slightly larger than that due to declining aerosols in CSIRO-Mk3.6 (panel a). An important difference between aerosols and long-lived GHGs is that declining BC in RCP45 leads to atmospheric radiative cooling ($-0.86\,W\,m^{-2}$), as opposed to atmospheric warming in the case of increasing long-lived GHGs ($+1.00\,W\,m^{-2}$). This implies that the "fast" precipitation response in RCP45 is negative for increasing long-lived GHGs and positive for declining aerosols; as we shall show in Sect. 4.2, this is reflected in a stronger response of global precipitation to declining aerosols. Also, the positive surface forcing due to declining aerosols is much larger than that due to increasing long-lived GHGs, which is also consistent with a stronger precipitation response in the aerosol case.

An interesting aspect of the atmospheric cooling induced by declining aerosols is that the ERF ($-0.86\,W\,m^{-2}$) is substantially weaker than the instantaneous direct effect ($-1.47\,W\,m^{-2}$). The shortwave component of the ERF is $-1.26\,W\,m^{-2}$, which is closer to the instantaneous value, but is still weaker by roughly $0.2\,W\,m^{-2}$. The difference is most substantial over East and Southeast Asia (not shown), where lower aerosol levels in the 2100 run strengthen the monsoon by perturbing the land-sea surface temperature gradient. This increases the column water vapour in this region, which increases atmospheric absorption of shortwave radiation. Cloud cover also increases, and this may enhance the effect by increasing multiple reflections between cloud layers. This perturbation of the land-sea surface temperature gradient may be (at least in part) artificial, since SSTs are fixed, while land-surface temperatures can change in these runs.

There is also a longwave adjustment of $+0.40\,W\,m^{-2}$ in the atmospheric ERF; this comprises a reduction of outgoing longwave radiation ($+0.13\,W\,m^{-2}$) due to a cooler at-





ACPD
13, 18621–18677, 2013



mosphere in response to reduced BC absorption, and net atmospheric warming at the lower boundary (+0.27 W m$^{-2}$), due to a cooler atmosphere and warming of the land-surface. The warmer surface may be seen as a limitation of the experimental design in the fixed-SST experiments, rather than a physically meaningful fast adjustment. Arguably, the ideal experimental design for evaluating aerosol ERF would use fixed SSTs and fixed land-surface temperatures, as demonstrated in a simplified GCM by Shine et al. (2003). However, implementing fixed land-surface temperatures in a consistent way is impractical (or at least difficult) for more complex climate models.

Figure 5 also shows the calculated radiative forcing for the NH and SH. The TOA ERF due to increasing long-lived GHGs is slightly smaller in the NH than in the SH, due to the larger proportion of land in the NH, which causes the atmosphere there to warm slightly due to a warmer land surface. Aerosol ERF is roughly twice as large in the NH as in the SH. This was previously shown for the TOA in Fig. 3, but Fig. 5 shows that this is also the case at the surface and in the atmosphere.

We did one further fixed-SST run to calculate the RCP4.5 "all forcing" ERF in 2100, i.e. aerosol emissions, ozone and long-lived GHG concentrations were all set to 2100 levels. Relative to 1850, this gave a TOA ERF of 3.87 W m$^{-2}$. This is somewhat less than the nominal forcing of 4.5 W m$^{-2}$, but it agrees well with the multi-model mean ERF for 2095 from Forster et al. (2013). They noted that ERF (which they calculated using the regression method, not fixed-SST runs) is generally less than radiative forcing, probably due to cloud adjustments.

## 4 Global and hemispheric climate response

In this section, we discuss simulated global and hemispheric changes in near-surface temperature and precipitation, with a primary focus on RCP4.5. Changes are quantified in terms of the least-squares trend, multiplied by the time period.





ACPD
13, 18621–18677, 2013



### 4.1 Surface temperature changes

Figure 6a shows anomalies of global-mean, near-surface temperature $T_s$ from the model and observations from HadCRUT4 (Morice et al., 2012). Prior to about 1980, the HIST ensemble mean mostly lies within the observational uncertainty, except for a period in the early 20th century, when the model appears to be too warm. (The plotted curves do not show the range of the 10-member ensembles; these are shown by Rotstayn et al., 2012.) HIST somewhat underestimates the observed warming towards the end of the historical period, although the model catches up in the last few years, due to the "hiatus" in the observed warming. In contrast, the NoAA ensemble mean (without the cooling effect of increasing AAs) substantially overestimates the increase in $T_s$.

In the 21st century, the difference between RCP45 and RCP45A2005 (black curve) shows that the warming effect of declining AAs is roughly 1 °C by 2100; this is similar to the result from Levy et al. (2013). The 2006–2100 linear warming trend due to declining AAs (1.1 °C per 95 yr) is a little less than half the total warming trend in RCP45 (2.3 °C per 95 yr). This is roughly in proportion to the TOA radiative forcing shown in Fig. 5, with aerosol ERF at the TOA slightly less than long-lived GHG ERF.

Another way to look at this is to note that RCP45A2005 shows slightly less warming by 2100 than RCP26 in CSIRO-Mk3.6; in other words, without the extra warming effect of declining AAs, RCP45 would warm less than RCP26. The surface temperature response in RCP26 is also similar to the effect of declining aerosols in RCP45; this is broadly consistent with little forcing due to changes in greenhouse gases in RCP2.6 (Van Vuuren et al., 2011) and net aerosol changes that are similar to those in RCP4.5 by 2100 (Fig. 1c).

Another feature of RCP45A2005 is that it shows a noticeable flattening of the warming rate after about 2065, although it occurs later and is less pronounced than in the strongly mitigated RCP26 experiment. In both RCP45A2005 and RCP26, the timing of





ACPD
13, 18621–18677, 2013



the flattening roughly corresponds to the flattening of the $CO_2$ concentration increase (Van Vuuren et al., 2011) (their Fig. 9).

Figure 6b compares changes in $T_s$ for the NH and SH. In RCP45A2005, the two hemispheres warm at similar rates (1.2 °C per 95 yr). The NH is expected to warm more rapidly than the SH under strong long-lived GHG forcing due to its larger proportion of land, and deep ocean mixing in the SH. However, a weakening of northward heat transport by the Atlantic meridional overturning circulation (AMOC) can exert the dominant control on the inter-hemispheric warming difference under moderate warming scenarios (Feulner et al., 2013). Our simulations do exhibit a strong "warming hole" over the mid-latitude North Atlantic (not shown), indicative of a substantial weakening of the AMOC (Drijfhout et al., 2012). This is also shown by Weaver et al. (2012) (their Fig. 2), in which the projected AMOC in CSIRO-Mk3.6 weakens more rapidly than in most other CMIP5 models.

In contrast, the projected warming due to declining AAs (black curves in Fig. 6b) is almost twice as strong in the NH compared to the SH. The linear trend (RCP45 minus RCP45A2005) is 1.45 °C per 95 yr in the NH and 0.76 °C per 95 yr in the SH. The ratio of warming between the hemispheres (1.9) is somewhat smaller than the inter-hemispheric forcing ratio (2.3). This difference may be due to a decrease of northward heat transport by the AMOC; historically increasing AAs have been shown to strengthen the AMOC in CSIRO-Mk3.6 (Collier et al., 2013), and the converse happens in response to declining AAs in RCP45 (figure not shown).

### 4.2 Precipitation changes

Simulated global-mean precipitation (Fig. 7a) shows little change in 2005 relative to 1850; the larger hydrological sensitivity to aerosol forcing explains why this can occur, despite an increase in global-mean temperature (Kloster et al., 2010). Reconstructions of historical precipitation are uncertain, but available evidence suggests that there is no clear long-term trend in global precipitation since 1950 (Balan Sarojini et al., 2012). In the model, substantial fluctuations during the historical period are associated with





ACPD
13, 18621–18677, 2013



volcanic eruptions (seen in NoAA as well as HIST) and strengthening aerosol effects between about 1960 and 1990.

In RCP45, global-mean precipitation increases by 0.16 mm per day in 95 yr (about 5.6 % of the model's climatological value). Of this, 63 % can be attributed to the effects of declining aerosols, and the remainder to increasing GHGs. This can be compared to the simulations of Levy et al. (2013) using GFDL-CM3; they obtained a global-mean precipitation increase of ∼ 0.15 mm per day in RCP4.5, with roughly half of this caused by declining aerosols.

For comparison, we again plot the curve from RCP26, in which the precipitation increase is slightly more than 0.1 mm per day in 95 yr, similar to the effect of declining aerosols in RCP45. As we found for global-mean $T_s$ (Fig. 6), this suggests that changes in RCP26 (with weak long-lived GHG forcing) are dominated by aerosol forcing.

Hemispheric means are plotted in Fig. 7b. In HIST, the precipitation decline between 1960 and 1990 is mainly a NH phenomenon, as is the relatively strong precipitation increase in RCP45. The NH RCP4.5 precipitation increase is mostly due to declining aerosols (72 %). Especially remarkable is that the 95 yr precipitation increase in RCP45 is roughly eight times as large in the NH (0.29 mm per day) as in the SH (0.037 mm per day).

Why is the inter-hemispheric ratio in precipitation change in RCP45 much larger than the inter-hemispheric ratio in radiative forcing or temperature change? In the NH, precipitation increases are driven by the fast and slow responses to declining aerosols, as discussed in Sect. 3.2. To a lesser extent, aerosol ERF also changes in the SH (Fig. 5), so one might expect SH precipitation to also increase. However, the 95 yr SH precipitation trend due to declining aerosols is essentially zero (–0.00 mm per day). The reason is that hemispheric precipitation changes are dominated by the tropics, and there is a northward shift of tropical precipitation as a dynamical response to declining aerosols.

The annual-mean meridional circulation change associated with the northward precipitation shift is shown in Fig. 8a. The anti-clockwise circulation trend (negative stream-





ACPD
13, 18621–18677, 2013



function change) implies anomalous ascent (subsidence) in the tropical NH (SH). This is of the opposite sign to the circulation change that has been found in simulations of the effects of historically increasing aerosols, both in CSIRO-Mk3.6 (Rotstayn et al., 2012) and other models (Williams et al., 2001; Ming and Ramaswamy, 2011). Note that energy transport by the Hadley circulation is in the direction of the upper branch (Chiang and Friedman, 2012; Hwang et al., 2013), so the anomalous circulation in Fig. 8a represents a net flux of energy from the NH to the SH.

The trend in tropical meridional circulation due to increasing greenhouse gases (Fig. 8b) is very different from the response to declining aerosols. Opposing circulation trends straddle the equator, representing increasing ascent in the equatorial zone, and compensating subsidence to the north and south. Increasing equatorial ascent in RCP45A2005 is a response to enhanced equatorial sea-surface warming, a common feature of climate projections forced by increasing greenhouse gases (Liu et al., 2005). This pattern is shown in Fig. 9 (red curve). It is in marked contrast to SST trends induced by declining aerosols (Fig. 9, blue curve). In the latter case, some equatorial enhancement is also seen, but the dominant feature is stronger warming in the NH compared to the SH, consistent with stronger aerosol forcing in the NH. This interhemispheric gradient in SST trends is reflected in the Hadley cell response to declining aerosols (Fig. 8a).

## 5 Other CMIP5 models

The above results suggest that projected 21st century warming in RCP4.5 will tend to be larger in CMIP5 models that have stronger (more negative) aerosol ERF in the present climate, as the aerosol ERF declines during the 21st century. They also suggest that precipitation changes in RCP4.5 may be substantially constrained by aerosol changes. We test this hypothesis by plotting projected and historical changes in temperature and precipitation against (2000 relative to 1850) aerosol ERF for 13 CMIP5 models, which are listed in Table 1. These are the models for which aerosol ERF (from





ACPD
13, 18621–18677, 2013



fixed-SST runs) was available for download at the time of writing, plus the ACCESS1.0 and ACCESS1.3 models (Bi et al., 2013; Dix et al., 2013) and GISS-E2-R (Shindell et al., 2013b). Temperature and precipitation changes are calculated from the least-squares trend, multiplied by the time period.

### 5.1 Global-mean temperature

In Fig. 10 we plot projected (2006–2100) and historical (1850–2005) changes in global-mean surface air temperature against aerosol ERF. The average aerosol ERF for the 13 models is $-1.15\,\mathrm{W\,m^{-2}}$. Models that include the second indirect effect tend to have more negative global-mean aerosol ERF; see Table 1. Although the magnitude (and possibly even the sign) of this effect in the real world is highly uncertain (e.g., Sandu et al., 2008), a decrease of precipitation efficiency with increasing aerosol concentration generally leads to an increase of cloud liquid water path in GCMs. This effect may be systematically over-predicted in GCMs, because they are unable to resolve other associated processes. For example, smaller cloud droplets in clouds affected by increased aerosol concentration may evaporate more readily, increasing the entrainment of dry air and thereby reducing cloud lifetime (Jiang et al., 2006). Such interactions are usually not resolved by the cloud schemes in current GCMs. Note that two models (MRI-CGCM3 and MIROC5) also include aerosol effects on ice clouds, though it is unclear how this influences the aerosol ERF in these models.

Figure 10a shows a significant correlation between aerosol ERF and projected warming in RCP4.5 ($r = -0.54$, $p = 0.03$). For comparison, panel b shows the correlation for the historical period, which is markedly stronger ($r = 0.87$). Aerosol ERF accounts for 76 % of the inter-model variance in simulated historical global-mean warming. The stronger correlation in the historical period presumably occurs because the net forcing is much weaker than in RCP4.5, so climate feedbacks are much weaker. Also, aerosol ERF is only available from these models for 2000 relative to 1850, so we have used these ERF values for RCP4.5 as well. The underlying assumption is that, to first order, aerosol ERF returns to its 1850 value by 2100, as it does in CSIRO-Mk3.6. However, in





ACPD
13, 18621–18677, 2013



reality there will be some variability among the models' aerosol ERF in 2100 (relative to 1850); this probably also contributes to the scatter seen in Fig. 10a.

Although the main focus of this paper is on RCP4.5, the good correlation between aerosol ERF and simulated historical warming suggests that this might provide a useful "top-down" estimate of aerosol ERF. The observed 1850–2005 surface warming from HadCRUT4 (Morice et al., 2012) is 0.66 °C, shown as the dashed horizontal line in Fig. 10b. The intersection of the regression line with the observed temperature change implies an estimated aerosol ERF of $-1.04\,W\,m^{-2}$, if this subset of CMIP5 models has no systematic bias in equilibrium climate sensitivity or ocean heat uptake.

Using a similar approach with several CMIP5 models, Shindell et al. (2013a) suggested that aerosol ERF of about –0.8 to $-1.5\,W\,m^{-2}$ is consistent with the observed historical warming; their uncertainty estimate incorporated the use of observed temperature change from two different data sets and different rates of warming in individual ensemble members in the CMIP5 models. The full uncertainty range for such top-down calculations may be even larger, due to uncertainties in observed temperature changes, climate sensitivity and ocean heat uptake. For example, Hansen et al. (2011) argued that their GCM (and many others) have excessive heat uptake by the deep ocean; after adjusting the temporal response function to account for this, they estimated aerosol forcing as $-1.6 \pm 0.3\,W\,m^{-2}$ by comparison with observational records. On the other hand, Libardoni and Forest (2011) found a much smaller aerosol forcing ($-0.19$ to $-0.83\,W\,m^{-2}$), with substantial sensitivity to the choice of observational data sets. A complementary approach uses satellite retrievals to constrain model calculations; for example, Quaas et al. (2009) estimated aerosol ERF as $-1.2 \pm 0.2\,W\,m^{-2}$.

Although the evidence presented in the previous paragraph is mixed, it seems more likely than not that our model's aerosol ERF at the TOA ($-1.4\,W\,m^{-2}$ in 2000) is too strong. On the other hand, CSIRO-Mk3.6 tends to underestimate atmospheric aerosol absorption of shortwave radiation, in common with other models (Shindell et al., 2013a). This is likely due to a combination of underestimated BC concentrations and underestimated absorption per unit mass (Koch et al., 2009).





ACPD
13, 18621–18677, 2013



### 5.2 Global-mean precipitation

Are changes in global precipitation similarly constrained by TOA aerosol ERF in these models? Figure 11 shows that for both RCP4.5 ($r = -0.56$) and the historical runs ($r = 0.83$), the correlation is comparable to what we found for temperature. In the historical runs, models with relatively strong aerosol ERF (less than about $-1.1\,\mathrm{W\,m^{-2}}$) tend to have negative precipitation changes, despite increasing global-mean $T_s$. This reflects the larger hydrological sensitivity for aerosol forcing compared to GHG forcing (Sect. 3.2).

According to the discussion in Sect. 3.2, the "fast" component of global precipitation change should respond to aerosol atmospheric ERF (i.e., atmospheric radiative heating). Since the fast component represents the part that is independent of changes in global-mean temperature, a useful way to represent this is via the hydrological sensitivity ($L\Delta P/\Delta T_s$; Pendergrass and Hartmann, 2012).

In Fig. 12 we plot this quantity against aerosol atmospheric ERF from the 13 CMIP5 models. This enables us to compare the range of hydrological sensitivity with that found by Pendergrass and Hartmann (2012) in CMIP3 projections, and also to test whether aerosol atmospheric ERF is a useful predictor of differences in hydrological sensitivity among the models. Note that the range of hydrological sensitivity in the historical runs is much larger than in RCP4.5, and includes positive and negative values. This reflects relatively small global-mean $T_s$ increases in the historical runs (Fig. 10b), and a mixture of positive and negative precipitation changes (Fig. 11b).

Pendergrass and Hartmann (2012) found an inter-model range of 0.6 to $2.1\,\mathrm{W\,m^{-2}\,K^{-1}}$ in hydrological sensitivity in CMIP3 projections forced by the SRES A1b scenario, which is a larger spread than shown for CMIP5 in Fig. 12a. The lower end of their range is much smaller than the lower end of the range in Fig. 12a ($1.5\,\mathrm{W\,m^{-2}\,K^{-1}}$). The reason is that there were no standardised BC emissions in CMIP3, and Pendergrass and Hartmann showed that the model with the smallest hydrological sensitivity was forced by *increasing* BC emissions during the 21st century. Except for one model





ACPD
13, 18621–18677, 2013



(MRI-CGCM3), the range in Fig. 12a is bounded by 1.5 to 2.1 $W m^{-2} K^{-1}$. A possible reason for the larger hydrological sensitivity in MRI-CGCM3 is that its aerosol ERF (both at the TOA and in the atmosphere) is large along the equator, especially in the vicinity of the maritime continent (not shown). This may drive a strong response of tropical deep convection in that model.

Figure 12 shows that in both RCP4.5 and the historical runs, the correlation of hydrological sensitivity with aerosol atmospheric ERF is not significant. However, $L\Delta P/\Delta T_s$ tends to vary in the direction expected, given that aerosol atmospheric heating increases in the historical runs and declines in RCP4.5. Several factors may contribute to the scatter in Fig. 12. As indicated in the previous paragraph, differences in the spatial patterns of aerosol ERF can be important, and the response of the models' convection schemes to the forcing is also likely to differ. Precipitation has a fast adjustment to long-lived GHG forcing, and this will differ among the models. Further, as implied by the discussion in Sect. 3.2, aerosol ERF calculated from fixed-SST simulations may have limitations as a predictor of the fast response of the atmosphere, due to changes in land-surface temperatures.

Few CMIP5 models include nitrate aerosol, and only one of the models we consider (GISS-E2-R) treats nitrate (Shindell et al., 2013b). Nitrate is expected to reduce the effect of declining aerosols, since emissions of ammonia from agriculture are assumed to increase in the RCPs (Van Vuuren et al., 2011; Bellouin et al., 2011; Lamarque et al., 2011). However, these increases are smaller in RCP4.5 than the other RCPs (Bellouin et al., 2011) (their Fig. 1).

Bellouin et al. (2011) calculated nitrate forcing for the four RCPs in a version of HadGEM2-ES. (Note that nitrate was not treated in the HadGEM2-ES CMIP5 runs.) In RCP4.5, they found that ammonium nitrate exerted (direct plus first indirect) forcing of $-0.2\,W m^{-2}$ in 2090 relative to 2000, somewhat less than the forcing they obtained for the other RCPs ($-0.3$ to $-0.5\,W m^{-2}$). Negative forcing was obtained in RCP4.5, despite relatively flat emissions of ammonia, due to competition between nitrate and sulfate precursors for a limited supply of ammonia.





ACPD
13, 18621–18677, 2013



The projected temperature and precipitation changes for GISS-E2-R are plotted below the regression lines in both Fig. 10a and Fig. 11a. In other words, its response is relatively subdued in RCP4.5, consistent with its inclusion of nitrate. However, it does not appear as an outlier relative to the other models, which suggests that inclusion of nitrate may not be a dominant factor that modulates the aerosol-induced response in RCP4.5. As indicated by Bellouin et al. (2011), nitrate is likely to be relatively more important in the other RCPs, in which it can substantially reduce the impact of decreasing $SO_2$ emissions.

### 5.3 Hemispheric means

In Fig. 13 we plot hemispheric-mean near-surface temperature changes against hemispheric-mean aerosol ERF. The average aerosol ERF across 12 models is $-1.73\,W\,m^{-2}$ in the NH and $-0.56\,W\,m^{-2}$ in the SH. The correlations are better in the NH than the SH, due to stronger aerosol forcing in the NH, though they are still significant in the SH. As seen for the global means, the correlations are also better in the historical experiments than in RCP4.5. All the models have larger warming in the NH than the SH in RCP4.5. This is not the case for several of the historical experiments, in which increasing aerosols tend to cool the NH relative to the SH.

Some of the scatter seen in RCP4.5 (panels a and c) is due to the fact that aerosol ERF in 2100 is not the same as in 1850. For example, the smallest NH warming in RCP4.5 is obtained from GISS-E2-R, which probably reflects the influence of nitrate in that model.

Top-down estimates of aerosol ERF are again shown by the vertical dashed lines, namely $-1.60\,W\,m^{-2}$ in the NH and $-0.42\,W\,m^{-2}$ in the SH. These are likely to be more uncertain than the global-mean estimates in Sect. 5.1.

Similar hemispheric scatter plots are shown for precipitation in Fig. 14. As expected, the correlation of both historical and projected precipitation changes with aerosol ERF is stronger in the historical experiments than in RCP4.5, and stronger in the NH than the SH. Correlations are highly significant in the NH, and in the SH the correlation is





ACPD
13, 18621–18677, 2013



significant at 5 %. Although the correlation in the SH is weak in RCP4.5 (panel c), it is worth noting that the regression line has a reversed slope compared to that in the NH (panel a). This suggests that, at least in some of the models, the SH precipitation response is partly controlled by compensating tropical subsidence relative to the NH (as we saw in CSIRO-Mk3.6). Such dynamic effects may reduce the correlation between SH aerosol ERF and SH precipitation changes.

## 6 Summary and conclusions

We focused on the medium-low RCP4.5 scenario, and assessed simulated global and hemispheric-scale effects of declining aerosols in CSIRO-Mk3.6. We also compared aspects of our results with other CMIP5 models for which estimates of aerosol ERF were available. Our simulations were forced by changes in emissions of sulfur dioxide, organic aerosol and black carbon from anthropogenic sources and biomass burning, and changing prescribed concentrations of long-lived GHGs and ozone.

We calculated the aerosol effective radiative forcing (ERF) using a series of atmospheric simulations with prescribed sea-surface temperatures, and compared the aerosol ERF with similar calculations of the ERF from increasing long-lived GHGs. We then compared two 10-member ensembles that used the coupled atmosphere-ocean version of the model. One (RCP45) was forced by the usual RCP4.5 during 2006–2100; the other (RCP45A2005) used identical forcing, except that emissions of anthropogenic aerosols and precursors were fixed at 2005 levels. Assuming linearity, the effects of declining aerosols were diagnosed from RCP45 minus RCP45A2005, while RCP45A2005 represented the effects of changes in GHGs. Since changes in tropospheric ozone are relatively small in RCP4.5, and our focus was on global and hemispheric-mean trends, to a good approximation RCP45A2005 represented the effects of increasing long-lived GHGs in RCP4.5.

Relative to 1850, global-mean aerosol ERF at the top of the atmosphere was $-1.40\,\mathrm{W\,m^{-2}}$ in 2000 and $-1.47\,\mathrm{W\,m^{-2}}$ in 2005. Relative to 2005, aerosol ERF was





ACPD
13, 18621–18677, 2013



1.46 W m$^{-2}$ in 2100, i.e., it approximately returned to 1850 levels. In our runs, increasing long-lived GHGs and declining aerosols exerted a positive ERF of similar magnitude at the top of the atmosphere between 2005 and 2100, but they had opposing effects on radiative heating within the atmosphere. Increasing GHGs exerted positive ERF in the atmosphere (+1.00 W m$^{-2}$), whereas declining aerosols exerted negative ERF (−0.86 W m$^{-2}$) due to reduced absorption of shortwave radiation by black carbon. This difference was also reflected in the corresponding ERF at the surface (+2.32 W m$^{-2}$ for declining aerosols, versus +0.54 W m$^{-2}$ for increasing long-lived GHGs).

The global-mean 2006–2100 projected surface warming in RCP45 was 2.3 °C, of which almost half (1.1 °C) was caused by declining aerosols. The warming due to declining aerosols was almost twice as strong in the NH as in the SH, whereas that due to increasing GHGs was similar in the two hemispheres.

Comparing declining aerosols with increasing GHGs, different radiative forcing at the surface and in the atmosphere had important implications for the hydrological cycle. For precipitation changes, the simulated effects of declining aerosols were substantially larger than those of increasing GHGs. Globally, 63 % of the projected 2006–2100 precipitation increase of 0.16 mm per day in RCP45 was caused by declining aerosols, and in the NH the corresponding proportion was even higher (72 %). The ratio of NH/SH precipitation change in RCP45 was much larger than suggested by the inter-hemispheric ratio in ERF: we showed that this was likely associated with changes in the Hadley circulation induced by declining aerosols: increasing ascent (subsidence) in the tropics of the NH (SH) increased the ratio of NH/SH precipitation change.

The above findings in a model with relatively strong present-day aerosol ERF raised interesting questions about similar effects in other CMIP5 models. Using data from 13 CMIP5 models (for which aerosol ERF could be calculated from fixed-SST experiments), we found that projected global-mean surface warming in RCP4.5 is systematically larger in models that have more negative aerosol ERF in the present climate ($r = -0.54$, $p = 0.03$). A similar correlation was found for global-mean precipitation changes ($r = -0.56$, $p = 0.02$). Analogous correlations were stronger in the historical





ACPD
13, 18621–18677, 2013



experiments, due to weaker net forcing ($r$ = 0.87 for surface temperature and $r$ = 0.83 for precipitation).

Considering hemispheric-mean changes in surface temperature and precipitation, correlations with aerosol ERF were stronger in the NH than the SH. Even in the SH, significant correlations were obtained between hemispheric-mean aerosol ERF and simulated surface temperature and precipitation changes. A clear exception was projected precipitation change in the SH, which suggested a degree of dynamical control from the Hadley circulation in the NH.

In RCP4.5, the hydrological sensitivity showed a smaller range than previously found for CMIP3 models forced by the A1b scenario (Pendergrass and Hartmann, 2012). This was explained by the fact that the CMIP5 models all have declining black carbon emissions in RCP4.5, whereas there was a mix of different assumptions about black carbon in CMIP3. However, aerosol atmospheric ERF was not especially skilful as a predictor of the models' hydrological sensitivity, and we suggested a number of possible reasons for this.

Aerosol ERF in 2100 was not available for the other CMIP5 models, and our approach was based on the tacit assumption that aerosol ERF returns to roughly 19th century values by 2100 in these models (as it did in CSIRO-Mk3.6). The extent to which this is true will vary among the models. For example, it may not be a good assumption for GISS-E2-R, which is the only model we considered that treats nitrate aerosol. Nitrate is expected to offset the effects of declines in other aerosol species, since emissions of ammonia from agriculture are projected to increase in the RCPs (though less so in RCP4.5 than in the other RCPs).

Our results suggest that the effects of declining aerosols in some respects resemble the effects of increasing GHGs, and in other respects are quite distinct. Thus, it is only partly accurate to think of declining aerosols as "unmasking" global warming, as asked in the title of this paper. Both forcings increase global-mean temperature, but aerosols act more strongly in the NH than the SH. Aside from stronger effects on surface temperature in the NH than the SH from aerosols, this also implies a different response of





ACPD
13, 18621–18677, 2013



atmospheric circulation for declining aerosols and increasing GHGs, which we showed for the Hadley circulation in Fig. 8. Recent work suggests that such changes in the Hadley circulation can affect the mid-latitude jet streams, especially in the SH in austral winter (Ceppi et al., 2013); in view of the distance of the SH eddy-driven jet from the location of strongest aerosol forcing in the NH, this is an intriguing topic for further research.

Further, the combination of positive TOA ERF and negative atmospheric ERF from declining aerosols implies a substantially stronger response of global precipitation than from increasing long-lived GHGs. This has previously been noted in near-term climate projections by Kloster et al. (2010). Although the larger hydrological sensitivity of aerosol forcing compared to long-lived GHGs has been discussed in a number of studies, it is perhaps more noticeable in these projections than in the more familiar case of historically increasing aerosols, because here both forcing agents contribute to global warming and increasing precipitation.

This paper has focused on aerosols, which contribute the largest uncertainty to radiative forcing. This compounds the uncertainty caused by climate feedbacks, especially those related to clouds (Dufresne and Bony, 2008). However, the effective radiative forcing due to increasing $CO_2$ also shows substantial variation among CMIP5 models, due to different rapid adjustments of the atmosphere and land surface (Andrews et al., 2012); this would also contribute to the scatter seen in Sect. 5.

Our results suggest that, in the medium-low RCP4.5 scenario, the response of CMIP5 models is substantially modulated by their present-day aerosol ERF. The relative importance of declining aerosols will presumably be smaller in RCP8.5, but larger in RCP2.6. Systematic efforts are needed to better quantify the role of declining aerosols in climate projections.

*Acknowledgements.* We thank Peter Vohralik for his careful reading of the manuscript, and Arnold Sullivan, Julie Noonan and Peter Vohralik for their work on the ACCESS forcing runs. L. Rotstayn and M. Collier were partly supported by the Australian Climate Change Science Program. We acknowledge the World Climate Research Programme's Working Group on Cou-





ACPD
13, 18621–18677, 2013



pled Modelling, which is responsible for CMIP, and we thank the climate modeling groups (listed in Table 1 of this paper) for producing and making available their model output. For CMIP the US Department of Energy's Program for Climate Model Diagnosis and Intercomparison provides coordinating support and led development of software infrastructure in partnership with the Global Organization for Earth System Science Portals.

## References

Ackerley, D., Booth, B. B. B., Knight, S. H. E., Highwood, E. J., Frame, D. J., Allen, M. R., and Rowell, D. P.: Sensitivity of 20th century Sahel rainfall to sulfate aerosol and $CO_2$ forcing, J. Climate, 24, 4999–5014, doi:10.1175/JCLI-D-11-00019.1, 2011. 18624

Allan, R. P., Liu, C., Zahn, M., Lavers, D. A., Koukouvagias, E., and Bodas-Salcedo, A.: Physically consistent responses of the global atmospheric hydrological cycle in models and observations, Surv. Geophys., 34, 1–20, doi:10.1007/s10712-012-9213-z, 2013. 18633

Allen, M. R. and Ingram, W. J.: Constraints on future changes in climate and the hydrologic cycle, Nature, 419, 224–232, 2002. 18633

Andreae, M. O. and Rosenfeld, D.: Aerosol–cloud–precipitation interactions. Part 1. The nature and sources of cloud-active aerosols, Earth-Sci. Rev., 89, 13–41, doi:10.1016/j.earscirev.2008.03.001, 2008. 18635

Andrews, T., Forster, P. M., and Gregory, J. M.: A surface energy perspective on climate change, J. Climate, 22, 2557–2570, doi:10.1175/2008JCLI2759.1, 2009. 18634

Andrews, T., Forster, P. M., Boucher, O., Bellouin, N., and Jones, A.: Precipitation, radiative forcing and global temperature change, Geophys. Res. Lett., 37, L14701, doi:10.1029/2010GL043991, 2010. 18633

Andrews, T., Gregory, J. M., Webb, M. J., and Taylor, K. E.: Precipitation, radiative forcing and global temperature change, Geophys. Res. Lett., 37, L09712, doi:10.1029/2012GL051607, 2012. 18650

Arblaster, J. M., Meehl, G. A., and Karoly, D. J.: Future climate change in the Southern Hemisphere: competing effects of ozone and greenhouse gases, Geophys. Res. Lett., 38, L02701, doi:10.1029/2010GL045384, 2011. 18629





ACPD
13, 18621–18677, 2013



Balan Sarojini, B., Stott, P. A., Black, E., and Polson, D.: Fingerprints of changes in annual and seasonal precipitation from CMIP5 models over land and ocean, Geophys. Res. Lett., 39, L21706, doi:10.1029/2012GL053373, 2012. 18639

Bellouin, N., Rae, J., Jones, A., Johnson, C., Haywood, J., and Boucher, O.: Aerosol forcing in the Climate Model Intercomparison Project (CMIP5) simulations by HadGEM2-ES and the role of ammonium nitrate, J. Geophys. Res., 116, D20206, doi:10.1029/2011JD016074, 2011. 18645, 18646

Bi, D., Dix, M., Marsland, S. J., O'Farrell, S., Rashid, H., Uotila, P., Hirst, A. C., Kowalczyk, E., Golebiewski, M., Sullivan, A., Yan, H., Hannah, N., Franklin, C., Sun, Z., Vohralik, P., Watterson, I., Zhou, X., Fiedler, R., Collier, M., Ma, Y., Noonan, J., Stevens, L., Uhe, P., Zhu, H., Griffies, S. M., Hill, R., Harris, C., and Puri, K.: The ACCESS coupled model: description, control climate and evaluation, Aust. Meteorol. Oceanogr. J., in press, 2013. 18642, 18663

Bollasina, M. A., Ming, Y., and Ramaswamy, V.: Anthropogenic aerosols and the weakening of the South Asian summer monsoon, Science, 334, 502–505, doi:10.1126/science.1204994, 2011. 18624

Booth, B. B. B., Dunstone, N. J., Halloran, P. R., Andrews, T., and Bellouin, N.: Aerosols implicated as a prime driver of twentieth-century North Atlantic climate variability, Nature, 484, 228–232, doi:10.1038/nature10946, 2012. 18624

Ceppi, P., Hwang, Y.-T., Liu, X., Frierson, D. M. W., and Hartmann, D. L.: The relationship between the ITCZ and the Southern Hemispheric eddy-driven jet, J. Geophys. Res.-Atmos., doi:10.1002/jgrd.50461, 2013. 18650

Chalmers, N., Highwood, E. J., Hawkins, E., Sutton, R., and Wilcox, L. J.: Aerosol contribution to the rapid warming of near-term climate under RCP 2.6, Geophys. Res. Lett., 39, L18709, doi:10.1029/2012GL052848, 2012. 18625

Cheng, Y., Lohmann, U., Zhang, J., Luo, Y., Liu, Z., and Lesins, G.: Contribution of changes in sea surface temperature and aerosol loading to the decreasing precipitation trend in southern China, J. Climate, 18, 1381–1390, 2005. 18624

Chiang, J. C. H. and Friedman, A. R.: Extratropical cooling, interhemispheric thermal gradients, and tropical climate change, Ann. Rev. Earth Pl. Sc., 40, 383–412, doi:10.1146/annurev-earth-042711-105545, 2012. 18624, 18641

Cionni, I., Eyring, V., Lamarque, J. F., Randel, W. J., Stevenson, D. S., Wu, F., Bodeker, G. E., Shepherd, T. G., Shindell, D. T., and Waugh, D. W.: Ozone database in support of CMIP5





ACPD
13, 18621–18677, 2013



simulations: results and corresponding radiative forcing, Atmos. Chem. Phys., 11, 11267–11292, doi:10.5194/acp-11-11267-2011, 2011. 18629

Collier, M. A., Rotstayn, L. D., Kim, K.-Y., Hirst, A. C., and Jeffrey, S. J.: Ocean circulation response to anthropogenic-aerosol and greenhouse-gas forcing in the CSIRO-Mk3.6.0 coupled climate model, Aust. Meteorol. Oceanogr. J., in press, 2013. 18639

Cooke, W. F., Liousse, C., Cachier, H., and Feichter, J.: Construction of a $1^{\circ} \times 1^{\circ}$ fossil fuel emission data set for carbonaceous aerosol and implementation and radiative impact in the ECHAM4 model, J. Geophys. Res., 104, 22137–22162, 1999. 18626

Dix, M., Vohralik, P., Bi, D., Rashid, H. A., Marsland, S. J., O'Farrell, S., Uotila, P., Hirst, A. C., Kowalcyzk, E. A., Sullivan, A., Yan, H., Franklin, C., Sun, Z., Watterson, I. G., Collier, M. A., Noonan, J., Rotstayn, L. D., Stevens, L., Uhe, P., and Puri, K.: The ACCESS coupled model: documentation of core CMIP5 simulations and initial results, Aust. Meteorol. Oceanogr. J., in press, 2013. 18642, 18663

Drijfhout, S., Van Oldenborgh, G. J., and Cimatoribus, A.: Is a decline of AMOC causing the warming hole above the North Atlantic in observed and modeled warming patterns?, J. Climate, 25, 8373–8379, doi:10.1175/JCLI-D-12-00490.1, 2012. 18639

Dufresne, J.-L. and Bony, S.: An assessment of the primary sources of spread of global warming estimates from coupled atmosphere ocean models, J. Climate, 21, 5135–5144, doi:10.1175/2008JCLI2239.1, 2008. 18650

Dufresne, J.-L., Foujols, M.-A., Denvil, S., Caubel, A., Marti, O., Aumont, O., Balkanski, Y., Bekki, S., Bellenger, H., Benshila, R., Bony, S., Bopp, L., Braconnot, P., Brockmann, P., Cadule, P., Cheruy, F., Codron, F., Cozic, A., Cugnet, D., de Noblet, N., Duvel, J.-P., Ethé, C., Fairhead, L., Fichefet, T., Flavoni, S., Friedlingstein, P., Grandpeix, J.-Y., Guez, L., Guilyardi, E., Hauglustaine, D., Hourdin, F., Idelkadi, A., Ghattas, J., Joussaume, S., Kageyama, M., Krinner, G., Labetoulle, S., Lahellec, A., Lefebvre, M.-P., Lefevre, F., Levy, C., Li, Z. X., Lloyd, J., Lott, F., Madec, G., Mancip, M., Marchand, M., Masson, S., Meurdesoif, Y., Mignot, J., Musat, I., Parouty, S., Polcher, J., Rio, C., Schulz, M., Swingedouw, D., Szopa, S., Talandier, C., Terray, P., and Viovy, N.: Climate change projections using the IPSL-CM5 Earth System Model: from CMIP3 to CMIP5, Climate Dynam., 40, 2123–2165, doi:10.1007/s00382-012-1636-1, 2013. 18663

Feichter, J., Kjellström, E., Rodhe, H., Dentener, F., Lelieveld, J., and Roelofs, G.-J.: Simulation of the tropospheric sulfur cycle in a global climate model, Atmos. Environ., 30, 1693–1707, 1996. 18626





ACPD
13, 18621–18677, 2013



Feichter, J., Roeckner, E., Lohmann, U., and Liepert, B.: Nonlinear aspects of the climate response to greenhouse gas and aerosol forcing, J. Climate, 17, 2384–2398, 2004. 18630

Feulner, G., Rahmstorf, S., Levermann, A., and Volkwardt, S.: On the Origin of the Surface Air Temperature Difference Between the Hemispheres in Earths Present-Day Climate, J. Climate, doi:10.1175/JCLI-D-12-00636.1, in press, 2013. 18639

Forster, P., Ramaswamy, V., Artaxo, P., Berntsen, T., Betts, R., Fahey, D., Haywood, J., Lean, J., Lowe, D., Myhre, G., Nganga, J., Prinn, R., Raga, G., Schulz, M., and Dorland, R. V.: Changes in atmospheric constituents and in radiative forcing, in: Climate Change 2007: The Physical Science Basis. Contribution of Working Group I to the Fourth Assessment Report of the Intergovernmental Panel on Climate Change, edited by: Solomon, S., Qin, D., Manning, M., Chen, Z., Marquis, M., Averyt, K. B., Tignor, M., and Miller, H. L., Cambridge University Press, Cambridge, UK and New York, NY, USA, 2007. 18623

Forster, P. M., Andrews, T., Good, P., Gregory, J. M., Jackson, L. S., and Zelinka, M.: Evaluating adjusted forcing and model spread for historical and future scenarios in the CMIP5 generation of climate models, J. Geophys. Res. Atmos., 118, 1139–1150, doi:10.1002/jgrd.50174, 2013. 18637

Gordon, H. B., Rotstayn, L. D., McGregor, J. L., Dix, M. R., Kowalczyk, E. A., O'Farrell, S. P., Waterman, L. J., Hirst, A. C., Wilson, S. G., Collier, M. A., Watterson, I. G., and Elliott, T. I.: The CSIRO Mk3 Climate System Model, Technical Paper No. 60, CSIRO Atmospheric Research, Aspendale, Vic., Australia, 134 pp., available at: http://www.cmar.csiro.au/e-print/open/gordon_2002a.pdf, 2002. 18626

Gordon, H. B., O'Farrell, S. P., Collier, M. A., Dix, M. R., Rotstayn, L. D., Kowalczyk, E. A., Hirst, A. C., and Watterson, I. G.: The CSIRO Mk3.5 Climate Model, Technical Report No. 21, The Centre for Australian Weather and Climate Research, Aspendale, Vic., Australia, 62 pp., available at: http://www.cawcr.gov.au/publications/technicalreports.php, 2010. 18626

Guenther, A., Hewitt, C. N., Erickson, D., Fall, R., Geron, C., Graedel, T., Harley, P., Klinger, L., Lerdau, M., McKay, W. A., Pierce, T., Scholes, B., Steinbrecher, R., Tallamraju, R., Taylor, J., and Zimmerman, P.: A global model of natural volatile organic compound emissions, J. Geophys. Res., 100, 8873–8892, 1995. 18627

Hansen, J., Sato, M., Kharecha, P., and von Schuckmann, K.: Earth's energy imbalance and implications, Atmos. Chem. Phys., 11, 13421–13449, doi:10.5194/acp-11-13421-2011, 2011. 18643





ACPD
13, 18621–18677, 2013



Hwang, Y.-T., Frierson, D. M. W., and Kang, S. M.: Anthropogenic sulfate aerosol and the southward shift of tropical precipitation in the late 20th century, Geophys. Res. Lett., 40, 2845–2850, doi:10.1002/grl.50502, 2013. 18641

Iversen, T., Bentsen, M., Bethke, I., Debernard, J. B., Kirkevåg, A., Seland, Ø., Drange, H., Kristjansson, J. E., Medhaug, I., Sand, M., and Seierstad, I. A.: The Norwegian Earth System Model, NorESM1-M – Part 2: Climate response and scenario projections, Geosci. Model Dev., 6, 389–415, doi:10.5194/gmd-6-389-2013, 2013. 18663

Jeffrey, S. J., Rotstayn, L. D., Collier, M. A., Dravitzki, S. M., Hamalainen, C., Moeseneder, C., Wong, K. K., and Syktus, J. I.: Australia's CMIP5 submission using the CSIRO Mk3.6 model, Aust. Meteorol. Oceanogr. J., in press, 2013. 18628, 18629, 18663

Jiang, H., Xue, H., Teller, A., Feingold, G., and Levin, Z.: Aerosol effects on the lifetime of shallow cumulus, Geophys. Res. Lett., 33, L14806, doi:10.1029/2006GL026024, 2006. 18642

Jones, A., Roberts, D. L., Woodage, M. J., and Johnson, C. E.: Indirect sulphate aerosol forcing in a climate model with an interactive sulphur cycle, J. Geophys. Res., 106, 20293–20310, 2001. 18627

Jones, C. D., Hughes, J. K., Bellouin, N., Hardiman, S. C., Jones, G. S., Knight, J., Liddicoat, S., O'Connor, F. M., Andres, R. J., Bell, C., Boo, K.-O., Bozzo, A., Butchart, N., Cadule, P., Corbin, K. D., Doutriaux-Boucher, M., Friedlingstein, P., Gornall, J., Gray, L., Halloran, P. R., Hurtt, G., Ingram, W. J., Lamarque, J.-F., Law, R. M., Meinshausen, M., Osprey, S., Palin, E. J., Parsons Chini, L., Raddatz, T., Sanderson, M. G., Sellar, A. A., Schurer, A., Valdes, P., Wood, N., Woodward, S., Yoshioka, M., and Zerroukat, M.: The HadGEM2-ES implementation of CMIP5 centennial simulations, Geosci. Model Dev., 4, 543–570, doi:10.5194/gmd-4-543-2011, 2011. 18663

Jones, G. S., Stott, P. A., and Christidis, N.: Attribution of observed historical near surface temperature variations to anthropogenic and natural causes using CMIP5 simulations, J. Geophys. Res., 118, 4001–4024, doi:10.1002/jgrd.50239, 2013. 18624

Kang, S. M., Frierson, D. M. W., and Held, I. M.: The tropical response to extratropical thermal forcing in an idealized GCM: the importance of radiative feedbacks and convective parameterization, J. Atmos. Sci., 66, 2812–2827, doi:10.1175/2009JAS2924.1, 2009. 18624

Kawase, H., Abe, M., Yamada, Y., Takemura, T., Yokohata, T., and Nozawa, T.: Physical mechanism of long-term drying trend over tropical North Africa, Geophys. Res. Lett., 37, L09706, doi:10.1029/2010GL043038, 2010. 18624





ACPD
13, 18621–18677, 2013



Kettle, A. J. and Andreae, M. O.: Flux of dimethylsulfide from the oceans: a comparison of updated data sets and flux models, J. Geophys. Res., 105, 26793–26808, 2000. 18627

Kirkevåg, A., Iversen, T., Seland, Ø., Hoose, C., Kristjánsson, J. E., Struthers, H., Ekman, A. M. L., Ghan, S., Griesfeller, J., Nilsson, E. D., and Schulz, M.: Aerosol–climate interactions in the Norwegian Earth System Model – NorESM1-M, Geosci. Model Dev., 6, 207–244, doi:10.5194/gmd-6-207-2013, 2013. 18663

Klimont, Z., Smith, S. J., and Cofala, J.: The last decade of global anthropogenic sulfur dioxide: 2000–2011 emissions, Environ. Res. Lett., 8, 014003, doi:10.1088/1748-9326/8/1/014003, 2013. 18630

Kloster, S., Dentener, F., Feichter, J., Raes, F., Lohmann, U., Roeckner, E., and Fischer-Bruns, I.: A GCM study of future climate response to aerosol pollution reductions, Climate Dynam., 34, 1177–1194, doi:10.1007/s00382-009-0573-0, 2010. 18625, 18634, 18639, 18650

Koch, D., Schulz, M., Kinne, S., McNaughton, C., Spackman, J. R., Balkanski, Y., Bauer, S., Berntsen, T., Bond, T. C., Boucher, O., Chin, M., Clarke, A., De Luca, N., Dentener, F., Diehl, T., Dubovik, O., Easter, R., Fahey, D. W., Feichter, J., Fillmore, D., Freitag, S., Ghan, S., Ginoux, P., Gong, S., Horowitz, L., Iversen, T., Kirkevåg, A., Klimont, Z., Kondo, Y., Krol, M., Liu, X., Miller, R., Montanaro, V., Moteki, N., Myhre, G., Penner, J. E., Perlwitz, J., Pitari, G., Reddy, S., Sahu, L., Sakamoto, H., Schuster, G., Schwarz, J. P., Seland, Ø., Stier, P., Takegawa, N., Takemura, T., Textor, C., van Aardenne, J. A., and Zhao, Y.: Evaluation of black carbon estimations in global aerosol models, Atmos. Chem. Phys., 9, 9001–9026, doi:10.5194/acp-9-9001-2009, 2009. 18643

Komuro, Y., Suzuki, T., Sakamoto, T. T., Hasumi, H., Ishii, M., Watanabe, M., Nozawa, T., Yokuhata, T., Nishimura, T., Ogochi, K., Emori, S., and Kimoto, M.: Sea-ice in twentieth-century simulations by new MIROC coupled models: a comparison between models with high resolution and with ice thickness distribution, J. Meteorol. Soc. Jpn., 90A, 213–232, doi:10.2151/jmsj.2012-A11, 2012. 18663

Lamarque, J.-F., Bond, T. C., Eyring, V., Granier, C., Heil, A., Klimont, Z., Lee, D., Liousse, C., Mieville, A., Owen, B., Schultz, M. G., Shindell, D., Smith, S. J., Stehfest, E., Van Aardenne, J., Cooper, O. R., Kainuma, M., Mahowald, N., McConnell, J. R., Naik, V., Riahi, K., and van Vuuren, D. P.: Historical (1850–2000) gridded anthropogenic and biomass burning emissions of reactive gases and aerosols: methodology and application, Atmos. Chem. Phys., 10, 7017–7039, doi:10.5194/acp-10-7017-2010, 2010. 18627





ACPD
13, 18621–18677, 2013



Lamarque, J.-F., Kyle, G. P., Meinshausen, M., Riahi, K., Smith, S. J., Vuuren, D. P., Conley, A. J., and Vitt, F.: Global and regional evolution of short-lived radiatively-active gases and aerosols in the Representative Concentration Pathways, Climatic Change, 109, 191–212, doi:10.1007/s10584-011-0155-0, 2011. 18623, 18627, 18645

Lee, S., Kim, H. K., Yan, B., Cobb, C. E., Hennigan, C., Nichols, S., Chamber, M., Edgerton, E. S., Jansen, J. J., Hu, Y., Zheng, M., Weber, R. J., and Russell, A. G.: Diagnosis of aged prescribed burning plumes impacting an urban area, Environ. Sci. Technol., 42, 1438–1444, doi:10.1021/es7023059, 2008. 18627

Levy II, H., Horowitz, L. W., Schwarzkopf, M. D., Ming, Y., Golaz, J.-C., Naik, V., and Ramaswamy, V.: The roles of aerosol direct and indirect effects in past and future climate change, J. Geophys. Res. Atmos., 118, 4521–4532, doi:10.1002/jgrd.50192, 2013. 18625, 18638, 18640, 18663

Libardoni, A. G. and Forest, C. E.: Sensitivity of distributions of climate system properties to the surface temperature dataset, Geophys. Res. Lett., 38, L22705, doi:10.1029/2011GL049431, 2011. 18643

Liepert, B. G., Feichter, J., Lohmann, U., and Roeckner, E.: Can aerosols spin down the water cycle in a warmer and moister world?, Geophys. Res. Lett., 31, L06207, doi:10.1029/2003GL019060, 2004. 18634

Liu, X., Xie, X., Yin, Z.-Y., Liu, C., and Gettelman, A.: A modeling study of the effects of aerosols on clouds and precipitation over East Asia, Theor. Appl. Climatol., 106, 343–354, doi:10.1007/s00704-011-0436-6, 2011. 18624

Liu, Z., Vavrus, S., He, F., Wen, N., and Zhong, Y.: Rethinking tropical ocean response to global warming: the enhanced equatorial warming, J. Climate, 18, 4684–4700, doi:10.1175/JCLI3579.1, 2005. 18641

The HadGEM2 Development Team: G. M. Martin, Bellouin, N., Collins, W. J., Culverwell, I. D., Halloran, P. R., Hardiman, S. C., Hinton, T. J., Jones, C. D., McDonald, R. E., McLaren, A. J., O'Connor, F. M., Roberts, M. J., Rodriguez, J. M., Woodward, S., Best, M. J., Brooks, M. E., Brown, A. R., Butchart, N., Dearden, C., Derbyshire, S. H., Dharssi, I., Doutriaux-Boucher, M., Edwards, J. M., Falloon, P. D., Gedney, N., Gray, L. J., Hewitt, H. T., Hobson, M., Huddleston, M. R., Hughes, J., Ineson, S., Ingram, W. J., James, P. M., Johns, T. C., Johnson, C. E., Jones, A., Jones, C. P., Joshi, M. M., Keen, A. B., Liddicoat, S., Lock, A. P., Maidens, A. V., Manners, J. C., Milton, S. F., Rae, J. G. L., Ridley, J. K., Sellar, A., Senior, C. A., Totterdell, I. J., Verhoef, A., Vidale, P. L., and Wiltshire, A.: The HadGEM2





ACPD
13, 18621–18677, 2013



family of Met Office Unified Model climate configurations, Geosci. Model Dev., 4, 723–757, doi:10.5194/gmd-4-723-2011, 2011. 18663
Meehl, G. A., Arblaster, J. M., and Collins, W. D.: Effects of black carbon aerosols on the Indian monsoon, J. Climate, 21, 2869–2882, doi:10.1175/2007JCLI1777.1, 2008. 18624
Menon, S., Hansen, J., Nazarenko, L., and Luo, Y.: Climate effects of black carbon aerosols in China and India, Science, 297, 2250–2253, 2002. 18624
Ming, Y. and Ramaswamy, V.: Nonlinear climate and hydrological responses to aerosol effects, J. Climate, 22, 1329–1339, doi:10.1175/2008JCLI2362.1, 2009. 18630
Ming, Y. and Ramaswamy, V.: A model investigation of aerosol-induced changes in tropical circulation, J. Climate, 24, 5125–5133, doi:10.1175/2011JCLI4108.1, 2011. 18624, 18641
Ming, Y., Ramaswamy, V., and Persad, G.: Two opposing effects of absorbing aerosols on global-mean precipitation, Geophys. Res. Lett., 37, L13701, doi:10.1029/2010GL042895, 2010. 18633, 18634
Morice, C. P., Kennedy, J. J., Rayner, N. A., and Jones, P. D.: Quantifying uncertainties in global and regional temperature change using an ensemble of observational estimates: the HadCRUT4 data set, J. Geophys. Res., 117, D08101, doi:10.1029/2011JD017187, 2012. 18638, 18643, 18669
Nakicenovic, N., Alcamo, J., Davis, G., de Vries, B., Fenhann, J., Gaffin, S., Gregory, K., Grubler, A., Jung, T. Y., Kram, T., Rovere, E. L. L., Michaelis, L., Mori, S., Morita, T., Pepper, W., Pitcher, H., Price, L., Riahi, K., Roehrl, A., Rogner, H.-H., Sankovski, A., Schlesinger, M., Shukla, P., Smith, S., Swart, R., van Rooijen, S., Victor, N., and Dadi, Z.: Emissions Scenarios. Special Report of the Intergovernmental Panel on Climate Change, Cambridge University Press, Cambridge, UK, 570 pp., 2000. 18623
O'Gorman, P. A. and Muller, C. J.: How closely do changes in surface and column water vapor follow Clausius–Clapeyron scaling in climate change simulations?, Environ. Res. Lett., 5, 025207, doi:10.1088/1748-9326/5/2/025207, 2010. 18632
O'Gorman, P. A., Allan, R. P., Byrne, M. P., and Previdi, M.: Energetic constraints on precipitation under climate change, Surv. Geophys., 33, 585–608, doi:10.1007/s10712-011-9159-6, 2012. 18633
Pendergrass, A. G. and Hartmann, D. L.: Global-mean precipitation and black carbon in AR4 simulations, Geophys. Res. Lett., 39, L01703, doi:10.1029/2011GL050067, 2012. 18644, 18649





ACPD
13, 18621–18677, 2013



Quaas, J., Ming, Y., Menon, S., Takemura, T., Wang, M., Penner, J. E., Gettelman, A., Lohmann, U., Bellouin, N., Boucher, O., Sayer, A. M., Thomas, G. E., McComiskey, A., Feingold, G., Hoose, C., Kristjánsson, J. E., Liu, X., Balkanski, Y., Donner, L. J., Ginoux, P. A., Stier, P., Grandey, B., Feichter, J., Sednev, I., Bauer, S. E., Koch, D., Grainger, R. G., Kirkevåg, A., Iversen, T., Seland, Ø., Easter, R., Ghan, S. J., Rasch, P. J., Morrison, H., Lamarque, J.-F., Iacono, M. J., Kinne, S., and Schulz, M.: Aerosol indirect effects – general circulation model intercomparison and evaluation with satellite data, Atmos. Chem. Phys., 9, 8697–8717, doi:10.5194/acp-9-8697-2009, 2009. 18643

Ramanathan, V., Chung, C., Kim, D., Bettge, T., Buja, L., Kiehl, J. T., Washington, W. M., Fu, Q., Sikka, D. R., and Wild, M.: Atmospheric brown clouds: impacts on South Asian climate and hydrological cycle, P. Natl. Acad. Sci., 102, 5326–5333, 2005. 18624

Roderick, M. L. and Farquhar, G. D.: The cause of decreased pan evaporation over the past 50 years, Science, 298, 1410–1411, 2002. 18634

Rotstayn, L. D.: A physically based scheme for the treatment of stratiform clouds and precipitation in large-scale models. I: Description and evaluation of the microphysical processes, Q. J. Roy. Meteor. Soc., 123, 1227–1282, 1997. 18628

Rotstayn, L. D.: Climate sensitivity of the CSIRO GCM: Effect of cloud modeling assumptions, J. Climate, 12, 334–356, 1999. 18628

Rotstayn, L. D. and Liu, Y.: A smaller global estimate of the second indirect aerosol effect, Geophys. Res. Lett., 32, L05708, doi:10.1029/2004GL021922, 2005. 18628

Rotstayn, L. D. and Liu, Y.: Cloud droplet spectral dispersion and the indirect aerosol effect: comparison of two treatments in a GCM, Geophys. Res. Lett., 36, L10801, doi:10.1029/2009GL038216, 2009. 18628

Rotstayn, L. D. and Lohmann, U.: Tropical rainfall trends and the indirect aerosol effect, J. Climate, 15, 2103–2116, doi:10.1175/1520-0442(2002)015<2103:TRTATI>2.0.CO;2, 2002a. 18624

Rotstayn, L. D. and Lohmann, U.: Simulation of the tropospheric sulfur cycle in a global model with a physically based cloud scheme, J. Geophys. Res., 107, 4592, doi:10.1029/2002JD002128, 2002b. 18626

Rotstayn, L. D., Ryan, B. F., and Penner, J. E.: Precipitation changes in a GCM resulting from the indirect effects of anthropogenic aerosols, Geophys. Res. Lett., 27, 3045–3048, doi:10.1029/2000GL011737, 2000. 18624





ACPD
13, 18621–18677, 2013



Rotstayn, L. D., Cai, W., Dix, M. R., Farquhar, G. D., Feng, Y., Ginoux, P., Herzog, M., Ito, A., Penner, J. E., Roderick, M. L., and Wang, M.: Have Australian rainfall and cloudiness increased due to the remote effects of Asian anthropogenic aerosols?, J. Geophys. Res., 112, D09202, doi:10.1029/2006JD007712, 2007. 18628

Rotstayn, L. D., Collier, M. A., Mitchell, R. M., Qin, Y., Campbell, S. K., and Dravitzki, S. M.: Simulated enhancement of ENSO-related rainfall variability due to Australian dust, Atmos. Chem. Phys., 11, 6575–6592, doi:10.5194/acp-11-6575-2011, 2011. 18628

Rotstayn, L. D., Jeffrey, S. J., Collier, M. A., Dravitzki, S. M., Hirst, A. C., Syktus, J. I., and Wong, K. K.: Aerosol- and greenhouse gas-induced changes in summer rainfall and circulation in the Australasian region: a study using single-forcing climate simulations, Atmos. Chem. Phys., 12, 6377–6404, doi:10.5194/acp-12-6377-2012, 2012. 18624, 18626, 18627, 18628, 18629, 18635, 18638, 18641, 18663

Rotstayn, L. D., Collier, M. A., Jeffrey, S. J., Kidston, J., Syktus, J. I., and Wong, K. K.: Anthropogenic effects on the subtropical jet in the Southern Hemisphere: aerosols versus long-lived greenhouse gases, Environ. Res. Lett., 8, 014030, doi:10.1088/1748-9326/8/1/014030, 2013. 18624

Sandu, I., Brenguier, J.-L., Geoffroy, O., Thouron, O., and Masson, V.: Aerosol impacts on the diurnal cycle of marine stratocumulus, J. Atmos. Sci., 65, 2705–2718, doi:10.1175/2008JAS2451.1, 2008. 18642

Sherwood, S. C., Ingram, W., Tsushima, Y., Satoh, M., Roberts, M., Vidale, P. L., and O'Gorman, P. A.: Relative humidity changes in a warmer climate, J. Geophys. Res., 115, D09104, doi:10.1029/2009JD012585, 2010. 18632

Shindell, D. T., Lamarque, J.-F., Schulz, M., Flanner, M., Jiao, C., Chin, M., Young, P. J., Lee, Y. H., Rotstayn, L., Mahowald, N., Milly, G., Faluvegi, G., Balkanski, Y., Collins, W. J., Conley, A. J., Dalsoren, S., Easter, R., Ghan, S., Horowitz, L., Liu, X., Myhre, G., Nagashima, T., Naik, V., Rumbold, S. T., Skeie, R., Sudo, K., Szopa, S., Takemura, T., Voulgarakis, A., Yoon, J.-H., and Lo, F.: Radiative forcing in the ACCMIP historical and future climate simulations, Atmos. Chem. Phys., 13, 2939–2974, doi:10.5194/acp-13-2939-2013, 2013a. 18627, 18628, 18629, 18631, 18633, 18635, 18636, 18643

Shindell, D. T., Pechony, O., Voulgarakis, A., Faluvegi, G., Nazarenko, L., Lamarque, J.-F., Bowman, K., Milly, G., Kovari, B., Ruedy, R., and Schmidt, G. A.: Interactive ozone and methane chemistry in GISS-E2 historical and future climate simulations, Atmos. Chem. Phys., 13, 2653–2689, doi:10.5194/acp-13-2653-2013, 2013b. 18642, 18645, 18663





ACPD
13, 18621–18677, 2013



Shine, K. P., Cook, J., Highwood, E. J., and Joshi, M. M.: An alternative to radiative forcing for estimating the relative importance of climate change mechanisms, Geophys. Res. Lett, 30, 2047, doi:10.1029/2003GL018141, 2003. 18637

Smith, S. J. and Bond, T. C.: Two hundred fifty years of aerosols and climate: the end of the age of aerosols, Atmos. Chem. Phys. Discuss., 13, 6419–6453, doi:10.5194/acpd-13-6419-2013, 2013. 18630

Smith, S. J., van Aardenne, J., Klimont, Z., Andres, R. J., Volke, A., and Delgado Arias, S.: Anthropogenic sulfur dioxide emissions: 1850–2005, Atmos. Chem. Phys., 11, 1101–1116, doi:10.5194/acp-11-1101-2011, 2011. 18630

Szopa, S., Balkanski, Y., Schulz, M., Bekki, S., Cugnet, D., Fortems-Cheiney, A., Turquety, S., Cozic, A., Déandreis, C., Hauglustaine, D., Idelkadi, A., Lathiére, J., Lefevre, F., Marchand, M., Vuolo, R., Yan, N., and Dufresne, J.-L.: Aerosol and ozone changes as forcing for climate evolution between 1850 and 2100, Climate Dynam., 40, 1–28, doi:10.1007/s00382-012-1408-y, 2013. 18663

Taylor, K. E., Stouffer, R. J., and Meehl, G. A.: An overview of CMIP5 and the experiment design, B. Am. Meteorol. Soc., 93, 485–498, doi:10.1175/BAMS-D-11-00094.1, 2012. 18623, 18633

Thomson, A. M., Calvin, K. V., Smith, S. J., Kyle, G. P., Volke, A., Patel, P., Delgado-Arias, S., Bond-Lamberty, B., Wise, M. A., Clarke, L. E., and Edmonds, J. A.: RCP4.5: A pathway for stabilization of radiative forcing by 2100, Climatic Change, 109, 77–94, doi:10.1007/s10584-011-0151-4, 2011. 18629, 18635

Van Vuuren, D. P., Edmonds, J., Kainuma, M., Riahi, K., Thomson, A., Hibbard, K., Hurtt, G. C., Kram, T., Krey, V., Lamarque, J.-F., Masui, T., Meinshausen, M., Nakicenovic, N., Smith, S. J., and Rose, S. K.: The representative concentration pathways: an overview, Climatic Change, 109, 5–31, doi:10.1007/s10584-011-0148-z, 2011. 18623, 18638, 18639, 18645

Villarini, G. and Vecchi, G. A.: Twenty-first-century projections of North Atlantic tropical storms from CMIP5 models, Nature Climate Change, 2, 604–607, doi:10.1038/nclimate1530, 2012. 18625

von Salzen, K., Scinocca, J. F., McFarlane, N. A., Li, J., Cole, J. N. S., Plummer, D., Verseghy, D., Reader, M. C., Ma, X., Lazare, M., and Solheim, L.: The Canadian Fourth Generation Atmospheric Global Climate Model (CanAM4). Part I: Representation of physical processes, Atmos. Ocean, 51, 104–125, doi:10.1080/07055900.2012.755610, 2013. 18663





ACPD
13, 18621–18677, 2013



Watanabe, M., Suzuki, T., O'Ishi, R., Komuro, Y., Watanabe, S., Emori, S., Takemura, T., Chikira, M., Ogura, T., Sekiguchi, M., Takata, K., Yamazaki, D., Yokohata, T., Nozawa, T., Hasumi, H., Tatebe, H., and Kimoto, M.: Improved climate simulation by MIROC5: mean states, variability, and climate sensitivity, J. Climate, 23, 6312–6335, doi:10.1175/2010JCLI3679.1, 2010. 18663

Weaver, A. J. Sedláček, J., Eby, M., Alexander, K., Crespin, E., Fichefet, T., Philippon-Berthier, G., Joos, F., Kawamiya, M., Matsumoto, K., Steinacher, M., Tachiiri, K., Tokos, K., Yoshimori, M., and Zickfeld, K.: Stability of the Atlantic meridional overturning circulation: a model intercomparison, Geophys. Res. Lett., 39, L20709, doi:10.1029/2012GL053763, 2012. 18639

Wigley, T. M. L.: Possible climate change due to $SO_2$-derived cloud condensation nuclei, Nature, 339, 365–367, doi:10.1038/339365a0, 1989. 18623

Williams, K. D., Jones, A., Roberts, D. L., Senior, C. A., and Woodage, M. J.: The response of the climate system to the indirect effects of anthropogenic sulfate aerosol, Climate Dynam., 17, 845–856, 2001. 18624, 18641

Xin, X., Wu, T., Li, J., Wang, Z., Li, W., and Wu, F.: How well does BCC_CSM1.1 reproduce the 20th century climate change over China?, Atmos. Ocean. Sci. Lett., 6, 21–26, 2013a. 18663

Xin, X., Zhang, L., Zhang, J., Wu, T., and Fang, Y.: Climate change projections over East Asia with BCC_CSM1.1 climate model under RCP scenarios, J. Meteorol. Soc. Jpn., in press, 2013b.

Yukimoto, S., Adachi, Y., Hosaka, M., Sakami, T., Yoshimura, H., Hirabara, M., Tanaka, T., Shindo, E., Tsujino, H., Deushi, M., Mizuta, R., Yabu, S., Obata, A., Nakano, H., Koshiro, T., Ose, T., and Kitoh, A.: A new global climate model of the Meteorological Research Institute: MRI-CGCM3 – model description and basic performance, J. Meteorol. Soc. Jpn., 90A, 23–64, doi:10.2151/jmsj.2012-A02, 2012. 18663





ACPD
13, 18621–18677, 2013



**Table 1.** Details of models used in Fig. 10 and subsequent figures.

| Model | Institution | Indirect effects[1] | Runs[2] | References |
|---|---|---|---|---|
| ACCESS1.0[3] | CSIRO (Commonwealth Scientific and Industrial Research Organisation) and Bureau of Meteorology, Australia | 2 | 2/1 | Bi et al. (2013); Dix et al. (2013) |
| ACCESS1.3[3] | CSIRO and Bureau of Meteorology, Australia | 2 | 3/1 | Bi et al. (2013); Dix et al. (2013) |
| BCC-CSM1.1 | Beijing Climate Center, China Meteorological Administration | 0 | 3/1 | Xin et al. (2013a,b) |
| CanESM2 | Canadian Centre for Climate Modelling and Analysis | 1 | 5/5 | von Salzen et al. (2013) |
| CSIRO-Mk3.6 | CSIRO with the Queensland Climate Change Centre of Excellence | 2 | 10/10 | Rotstayn et al. (2012); Jeffrey et al. (2013) |
| GFDL-CM3 | Geophysical Fluid Dynamics Laboratory | 2 | 5/1 | Levy et al. (2013) |
| GISS-E2-R[4] | NASA Goddard Institute for Space Studies | 1 | 6/6 | Shindell et al. (2013b) |
| HadGEM2-AO[5] | Met Office Hadley Centre | 2 | 1/1 | Jones et al. (2011); Martin et al. (2011) |
| HadGEM2-ES[5] | Met Office Hadley Centre | 2 | 5/4 | Jones et al. (2011); Martin et al. (2011) |
| IPSL-CM5A-LR | Institut Pierre-Simon Laplace | 1 | 6/4 | Dufresne et al. (2013); Szopa et al. (2013) |
| MIROC5 | Atmosphere and Ocean Research Institute, National Institute for Environmental Studies, and Japan Agency for Marine-Earth Science and Technology | 3 | 5/3 | Watanabe et al. (2010); Komuro et al. (2012) |
| MRI-CGCM3 | Meteorological Research Institute | 3 | 3/1 | Yukimoto et al. (2012) |
| NorESM1-M | Norwegian Climate Centre | 2 | 3/1 | Iversen et al. (2013); Kirkevåg et al. (2013) |

[1] Indirect aerosol effects: 0 denotes no aerosol-cloud interaction; 1 denotes the cloud-albedo effect; 2 denotes 1 plus an effect on warm-rain formation; 3 denotes 2 plus an effect on ice clouds.
[2] Number of historical and RCP4.5 ensemble members, respectively.
[3] Unpublished aerosol ERFs from ACCESS1.0 and ACCESS1.3 provided by P. Vohralik (personal communication, 2013).
[4] Unpublished aerosol ERFs from GISS-E2-R (physics version 3) provided by D. Shindell (personal communication, 2013). GISS-E2-R includes nitrate.
[5] Aerosol ERF for HadGEM2-AO and HadGEM2-ES is identical. Differences between HadGEM2-AO and HadGEM2-ES include the treatment of ozone and inclusion of dynamic vegetation in HadGEM2-ES. Historical trends are calculated from 1860 in HadGEM2-AO and HadGEM2-ES.





ACPD
13, 18621–18677, 2013



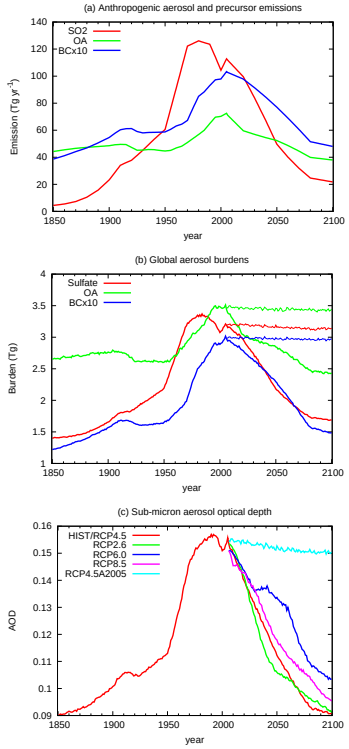


**Fig. 1.** Time series of global, annual-mean aerosol properties: **(a)** anthropogenic emissions of $SO_2$ (red), OA (green) and BC (blue, multiplied by 10), shown as teragrams of species. **(b)** Global aerosol burdens from HIST (1850–2005) and RCP45 (2006–2100), shown as thick lines: sulfate (red), OA (green) and BC (blue, multiplied by 10). Corresponding burdens from RCP45A2005 (2006–2100) are shown as thin lines. **(c)** Sub-micron clear-sky AOD at 550 nm from HIST and RCP45 (red line), comprising the sum of AOD from sulfate, OA and BC. For comparison, AODs for 2006–2100 are also shown for RCP45A2005 and the other standard RCPs.





ACPD
13, 18621–18677, 2013



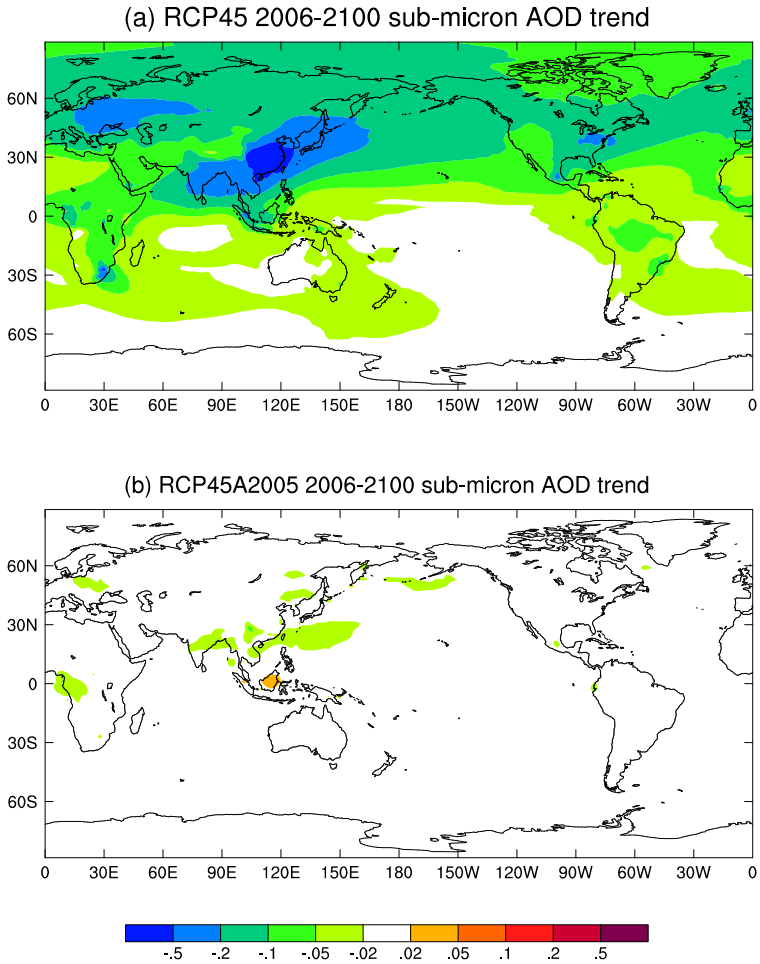


**Fig. 2.** 2006–2100 trends of annual-mean, sub-micron clear-sky AOD at 550 nm (AOD units per century) from **(a)** RCP45, and **(b)** RCP45A2005.





ACPD
13, 18621–18677, 2013



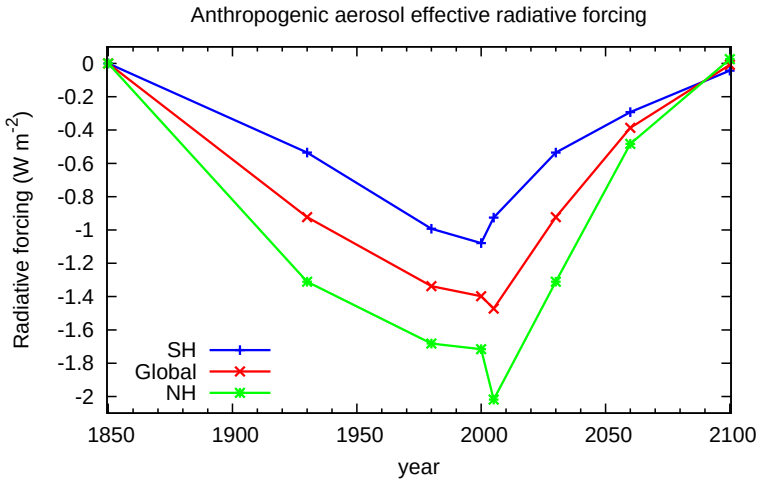


**Fig. 3.** Anthropogenic aerosol effective radiative forcing for the historical period and RCP4.5, averaged over the SH (blue line), the globe (red line) and the NH (green line). Calculations are for years 1850, 1930, 1980, 2000, 2005, 2030, 2060 and 2100, with linear interpolation in between.





ACPD
13, 18621–18677, 2013



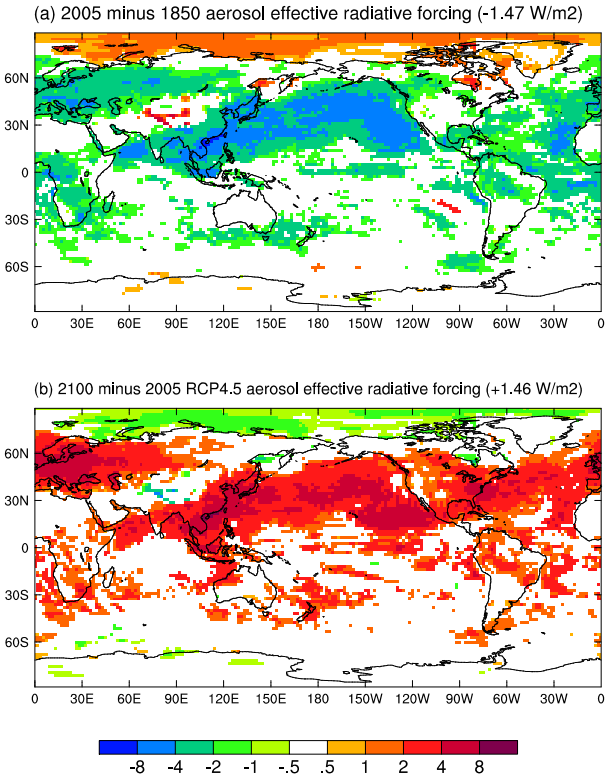


**Fig. 4.** Aerosol effective radiative forcing at the top of the atmosphere ($W\,m^{-2}$): **(a)** 2005 minus 1850, **(b)** 2100 minus 2005. Shaded regions show ERF values that are significantly different from zero at 5 %, based on a two-sample *t* test.





ACPD
13, 18621–18677, 2013



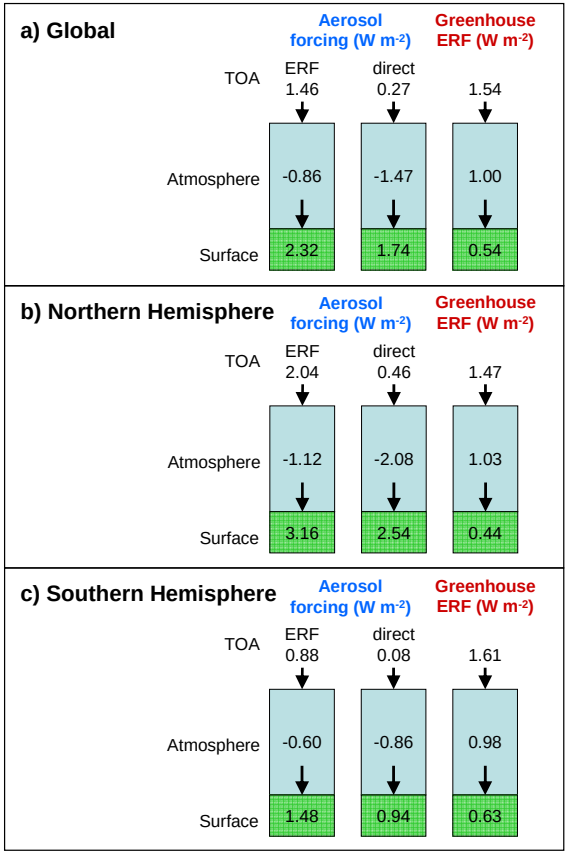


**Fig. 5.** Radiative forcing at the TOA, in the atmosphere, and at the surface for 2100 minus 2005 in RCP4.5, calculated from fixed-SST simulations: **(a)** global-mean, **(b)** Northern Hemisphere, **(c)** Southern Hemisphere. The first two columns show the total aerosol ERF and the (instantaneous) direct radiative forcing. The third column shows the ERF for long-lived GHGs.





ACPD
13, 18621–18677, 2013



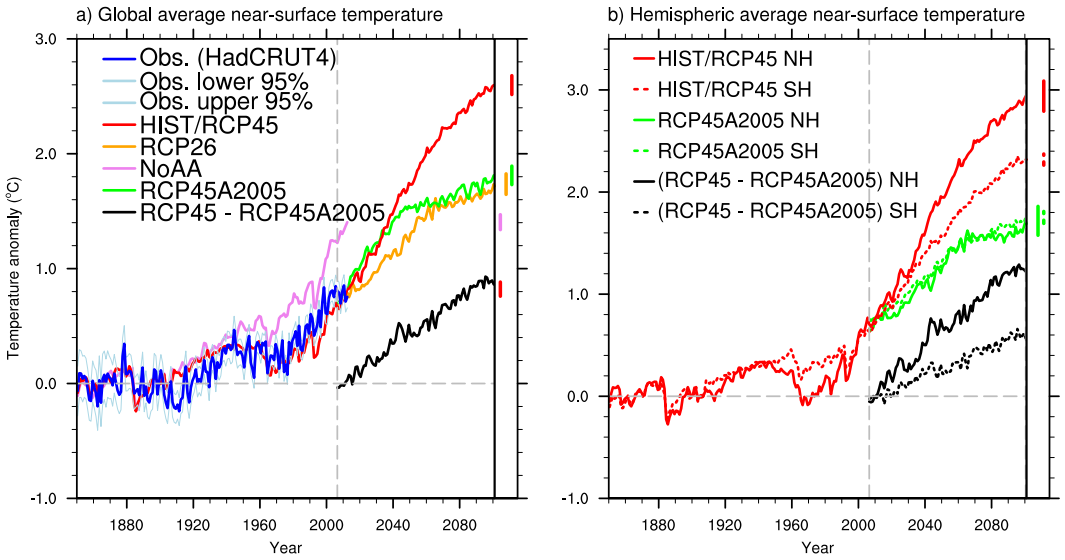


**Fig. 6. (a)** Anomalies (relative to the 1850–1899 mean) of annual-mean, ensemble-mean near-surface temperature: **(a)** global means, **(b)** NH and SH means. In panel a, the thick blue curve shows observations for 1850–2012 (HadCRUT4; Morice et al., 2012). The thin light blue curves denote 95 % uncertainty bounds for the observations. In both panels, differences between RCP45 and RCP45A2005 are shown as black curves, and the vertical dashed line at 2006 marks the start of the projections. The vertical bars in the right inset show the standard deviations of the mean temperature from the last 10 yr of each experiment (2091–2100 for the projections, or 2003–2012 for HIST and NoAA).





ACPD
13, 18621–18677, 2013



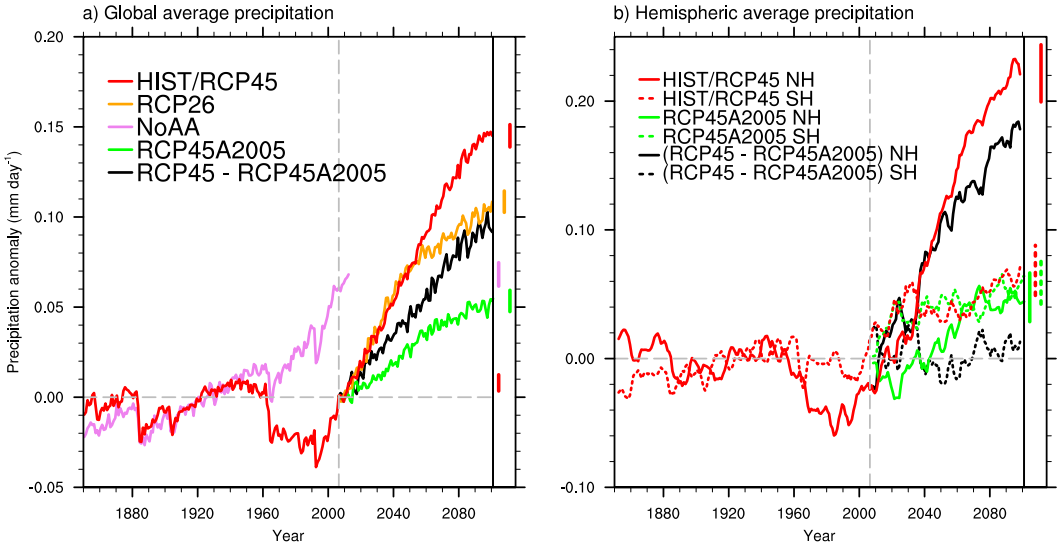


**Fig. 7.** Anomalies (relative to the 1850–1899 mean) of annual-mean, ensemble-mean precipitation from the model: **(a)** global means, **(b)** NH and SH means. In both panels, differences between RCP45 and RCP45A2005 are shown as black curves, and the vertical dashed line at 2006 marks the start of the projections. The vertical bars in the right inset show the standard deviations of the mean precipitation from the last 10 yr of each experiment (2091–2100 for the projections, or 2003–2012 for HIST and NoAA). In **b**, a five-year running mean was applied to reduce noise.





ACPD
13, 18621–18677, 2013



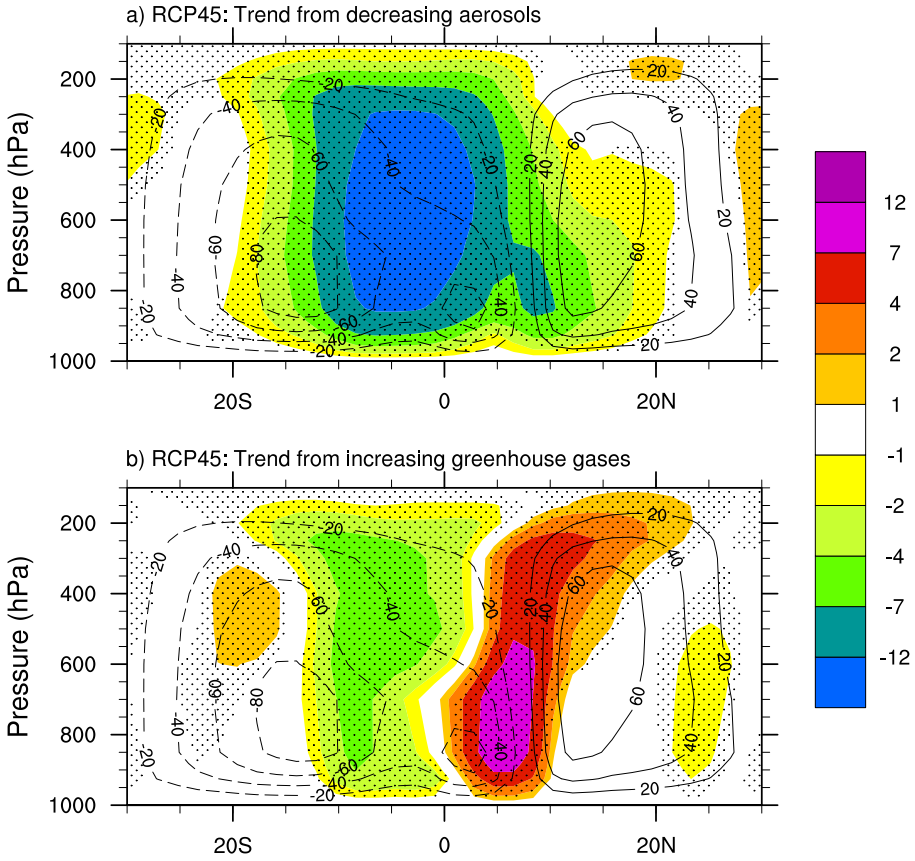


**Fig. 8.** 2006–2100 trends ($10^9$ kg s$^{-1}$ per century) in annual-mean meridional streamfunction (shaded) from **(a)** RCP45 minus RCP45A2005, and **(b)** RCP45A2005. Contours show the climatology from HIST, averaged over 1986–2005 ($10^9$ kg s$^{-1}$). Positive numbers denote clockwise circulation. Stippling denotes changes significant at 5 %, based on a two-sided *t* test.





ACPD
13, 18621–18677, 2013



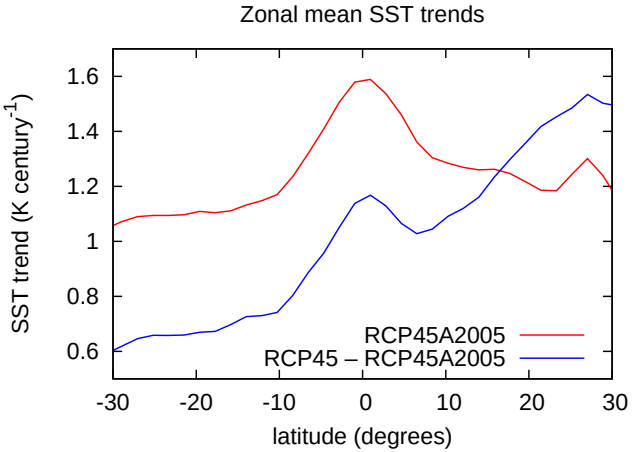


**Fig. 9.** 2006–2100 zonal-mean SST trends at low latitudes from RCP45A2005 (red curve) and RCP45 minus RCP45A2005 (blue curve).





ACPD
13, 18621–18677, 2013



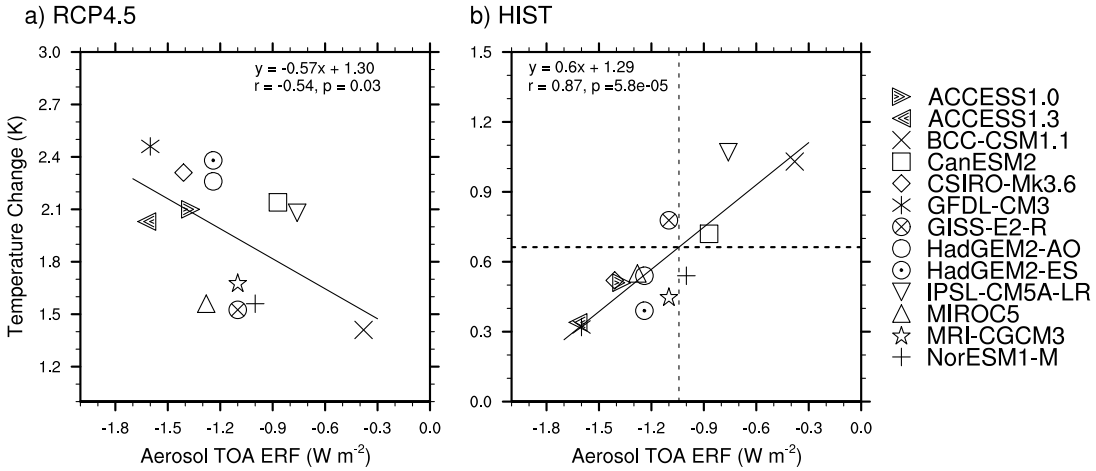


**Fig. 10.** Changes in global-mean surface-air temperature from CMIP5 models plotted against (2000 relative to 1850) global-mean aerosol ERF diagnosed from fixed-SST simulations: **(a)** RCP4.5 (2006–2100), **(b)** historical simulations (1850–2005). CMIP5 models are listed in Table 1. Temperature changes are calculated from least-squares trends. The dashed horizontal line in **(b)** shows the observed 1850–2005 warming from HadCRUT4, and the dashed vertical line shows the "top-down" estimate of aerosol ERF implied by the intersection of the horizontal line with the regression line.





ACPD
13, 18621–18677, 2013



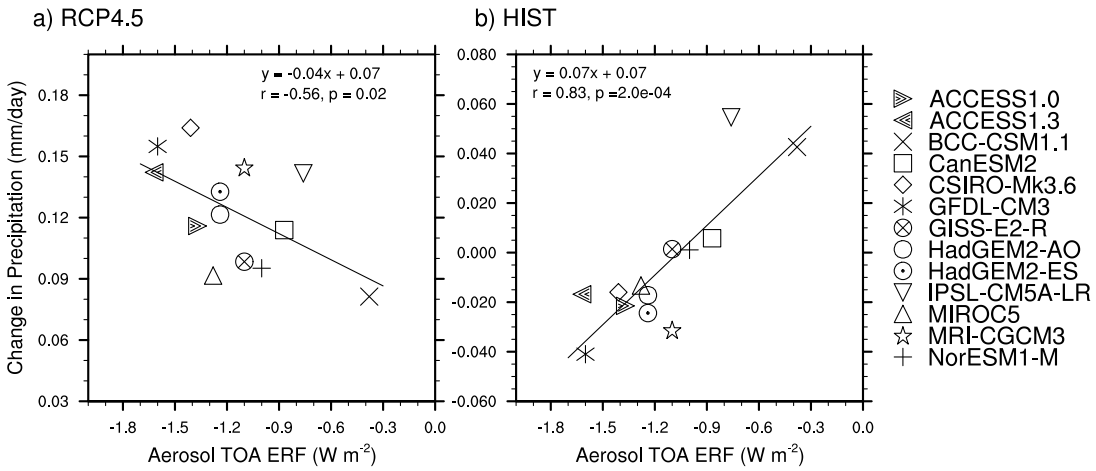


**Fig. 11.** Changes in global-mean precipitation from CMIP5 models plotted against (2000 relative to 1850) global-mean aerosol ERF diagnosed from fixed-SST simulations: **(a)** RCP4.5 (2006–2100), **(b)** historical simulations (1850–2005). Precipitation changes are calculated from least-squares trends.





ACPD
13, 18621–18677, 2013



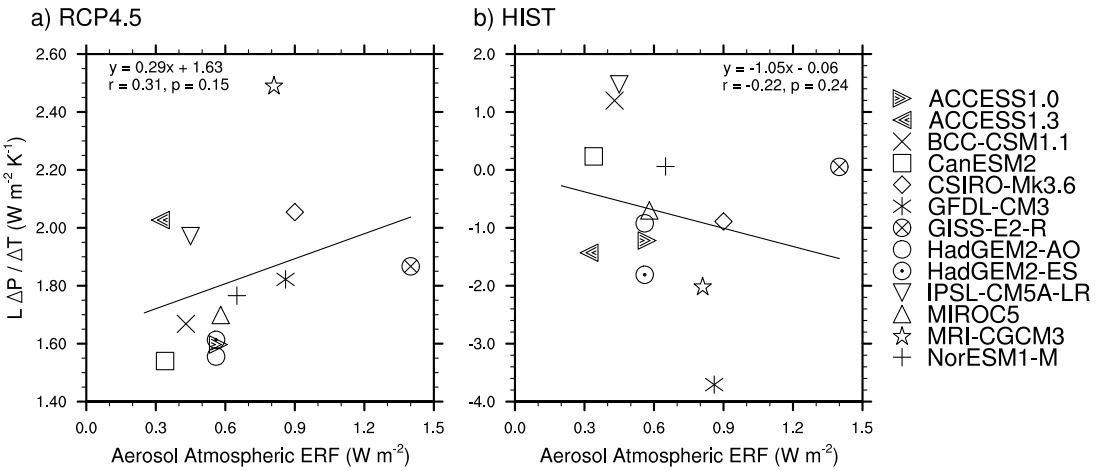


**Fig. 12.** Hydrological sensitivity ($L\Delta P/\Delta T_s$) from CMIP5 models plotted against (2000 relative to 1850) global-mean aerosol ERF diagnosed from fixed-SST simulations: **(a)** RCP4.5 (2006–2100), **(b)** historical simulations (1850–2005). Precipitation and temperature changes are calculated from least-squares trends.





ACPD
13, 18621–18677, 2013



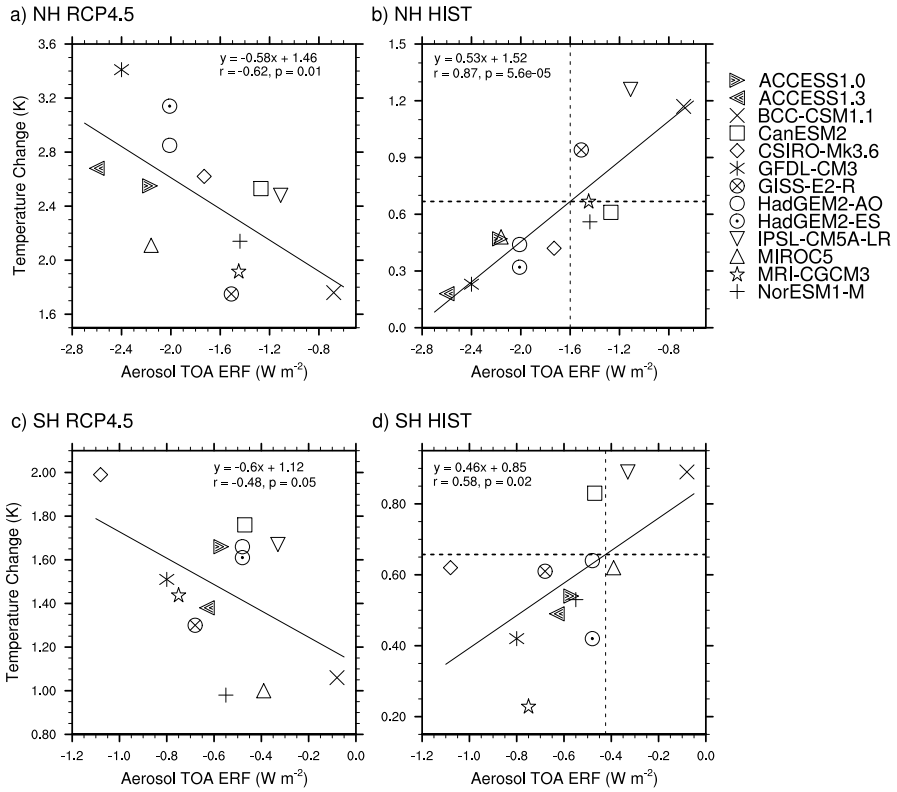


**Fig. 13.** Changes in hemispheric-mean surface-air temperature from CMIP5 models plotted against (2000 relative to 1850) hemispheric-mean aerosol ERF diagnosed from fixed-SST simulations: **(a)** NH RCP4.5, **(b)** NH historical simulations, **(c)** SH RCP4.5, **(d)** SH historical simulations. The dashed horizontal lines in panels **(b)** and **(d)** show the observed 1850–2005 hemispheric-mean warming from HadCRUT4, and the dashed vertical lines show the "top-down" estimate of aerosol ERF implied by the intersection of the horizontal lines with the regression lines.





ACPD
13, 18621–18677, 2013



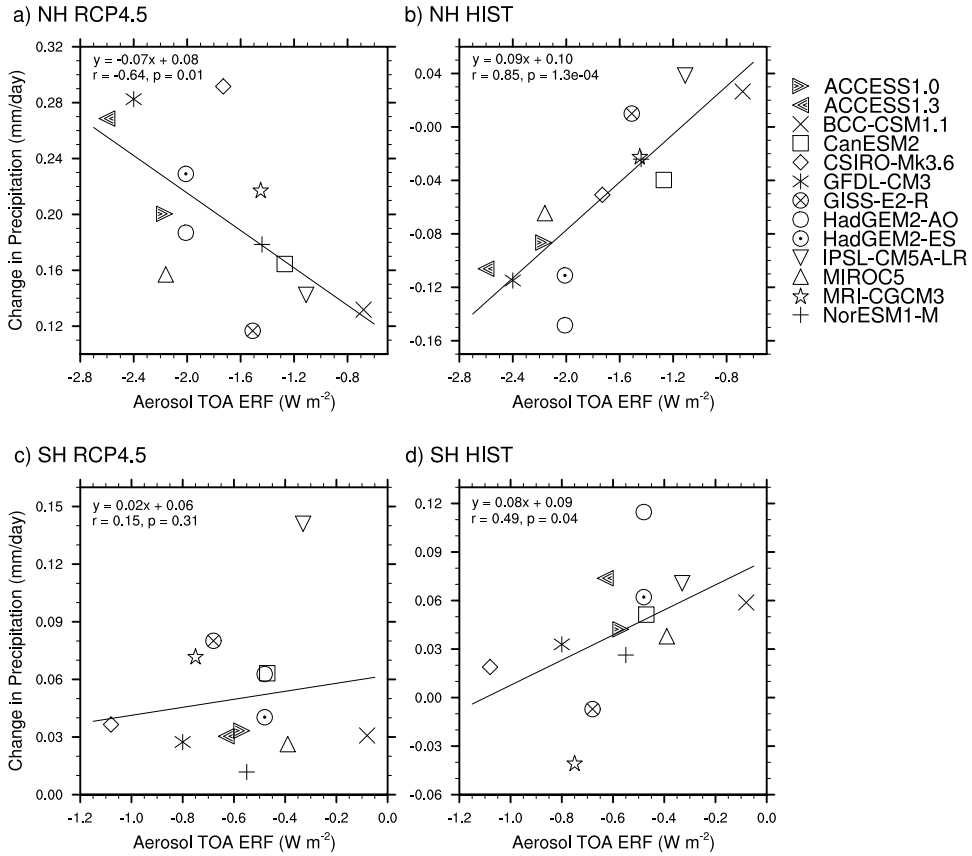


**Fig. 14.** Changes in hemispheric-mean precipitation from CMIP5 models plotted against (2000 relative to 1850) hemispheric-mean aerosol ERF diagnosed from fixed-SST simulations: **(a)** NH RCP4.5, **(b)** NH historical simulations, **(c)** SH RCP4.5, **(d)** SH historical simulations.





ACPD
13, 18621–18677, 2013